An ensemble three-dimensional variational data assimilation system for the global ocean: sensitivity to the observation- and background-error variance formulation

N. Daget[1], A. T. Weaver[1] and M. A. Balmaseda[2]

Research Department

[1]Centre Européen de Recherche et de Formation Avancée en Calcul Scientifique, Toulouse, France
[2]European Centre for Medium-Range Weather Forecasts, Reading, United Kingdom

June 2008

European Centre for Medium-Range Weather Forecasts
Europäisches Zentrum für mittelfristige Wettervorhersage
Centre européen pour les prévisions météorologiques à moyen terme

1   Abstract

This paper presents a three-dimensional variational data assimilation (3D-Var) system that has been developed for global analysis with the OPA ocean general circulation model. The global 3D-Var system is based on an earlier system developed for the tropical Pacific, but has been extended to incorporate new features including fully multivariate background-error covariances and the capacity to produce ensembles of ocean analyses for climate studies and forecast initialization. The ensembles are created by perturbing the surface forcing fields (wind-stress, fresh-water flux and heat flux) and the observations (temperature and salinity profiles) used in the assimilation process.

Cycled 3D-Var experiments over the period 1993-2000 are presented to test the sensitivity of the analyses to two flow-dependent formulations of the background-error standard deviations (σ^b) for temperature and salinity. The first formulation is based on an empirical parameterization of σ^b in terms of the vertical gradients of the background temperature and salinity fields, while the second formulation involves a more sophisticated approach that derives σ^b from the spread of an ensemble of analyses. In both experiments, the observation-error standard deviations (σ^o) are geographically dependent and estimated from a model-data comparison prior to assimilation. An additional 3D-Var experiment that employs the parameterized σ^b but a simpler σ^o formulation, and a control experiment involving no data assimilation were also conducted and used for comparison.

All 3D-Var experiments produce a significant reduction in the mean and standard deviation of the temperature and salinity innovations compared to those of the control experiment. Comparing innovation statistics from the two σ^b formulations shows that both formulations produce similar results below approximately 150 m but the parameterized σ^b produce slightly better results above this depth where statistical consistency checks indicate that the ensemble σ^b are underestimated. The rate at which observational information is lost between cycles, however, is shown to be much reduced with the ensemble σ^b, suggesting that the analyses produced with the ensemble σ^b are in better balance than those produced with the parameterized σ^b. Sea surface height (SSH) anomalies in the northwest Atlantic and zonal velocities in the equatorial Pacific, which are fields not directly constrained by the observations, are clearly better with the ensemble σ^b than with the parameterized σ^b when compared to independent data. Results show that while some aspects of those variables are improved with data assimilation (SSH anomalies and currents in the central and eastern Pacific), other aspects are degraded (SSH anomalies in the northwest Atlantic, currents in the western Pacific). Areas for improving the ensemble method and for making better use of the ensemble information are discussed.

2 Introduction

A variational data assimilation system for the OPA ocean general circulation model (Madec *et al.* 1998) has been developed at CERFACS for climate research applications. The system, known as OPAVAR, is based on an incremental variational algorithm (Courtier *et al.* 1994). Three- and four-dimensional variational assimilation (3D-Var and 4D-Var) versions of the system were initially developed for tropical Pacific basin applications (Weaver *et al.* 2003; Vialard *et al.* 2003; Ricci *et al.* 2005). The system was later extended to a global configuration in the European ENACT[1] project where it was applied to produce multi-decadal ocean analyses for seasonal hindcast initialization and studies of ocean climate variability (Davey *et al.* 2006; Carton and Santorelli 2008). Important advances were made to the system during ENACT, one of the most noteworthy being the development of a fully multivariate background-error covariance model based on balance operators (Weaver *et al.* 2005). More recently the system has been extended in the European ENSEMBLES[2] project to generate a nine-member ensemble of multi-decadal ocean analyses. The ensemble was produced using multiple atmospheric forcing fields whose differences were constructed to be consistent with estimates of the actual uncertainty in these fields. In ENSEMBLES, the ocean analysis ensemble has been used to contribute to the production of probabilistic forecasts on seasonal to decadal times scales (Weisheimer *et al.* 2007).

The important feature of an ensemble data assimilation system is its capacity to provide flow-dependent information on analysis and background error. This information can be exploited in a cycled assimilation system to improve the estimate of the background-error covariance matrix on each cycle, although no attempt was made to do this in the ENSEMBLES experiments. The simplest way to use the ensemble information is to build a low-rank approximation to the background-error covariance matrix on a given cycle from the sample covariance of the ensemble of model forecast states initiated from the previous cycle. The matrix is rank deficient since the number of ensemble members is typically several orders of magnitude smaller than the number of background state variables. In the Ensemble Kalman Filter (EnKF), this rank deficiency can be exploited to produce computationally efficient implementations of the standard Kalman filter analysis equation (see Houtekamer and Mitchell (2005) and Evensen (2007) for a review of the different variants of the EnKF). However, using a small ensemble to estimate the covariance matrix directly in a high-dimensional system can lead to noisy variances and spurious long-range correlations due to sampling error. Various filtering and localization procedures have been proposed to alleviate this problem in practical implementations of the EnKF (Houtekammer and Mitchell 2001; Keppenne and Reinecker 2002; Ott *et al.* 2004; Buehner and Charron 2007; Oke *et al.* 2007).

Lorenc (2003b) and Buehner (2005) illustrate how an ensemble-estimated background-error covariance matrix, with or without localization, can be used in a variational assimilation scheme. The procedure involves using the square root of the (localized) ensemble covariance matrix to transform the control vector into a vector of background-state increments. The basic transformation is designed to precondition the minimization problem and is standard in variational assimilation systems that employ more conventional background-error covariance formulations based on covariance models (Derber and Bouttier 1999; Lorenc 2003a; Weaver *et al.* 2005). Methods to define the background-error covariance matrix as a linear combination of an ensemble-estimated matrix and a covariance model matrix have also been proposed (Hamill and Synder 2000; Lorenc 2003b; Buehner 2005).

Rather than using the ensemble directly to construct an estimate of the covariance matrix, it may be used indirectly to calibrate specific parameters of a covariance model (Fisher 2003; Žagar *et al.* 2005; Belo Pereira and Berre 2006; Berre *et al.* 2006). The use of a covariance model has the advantage of providing a full-

---

[1]ENhanced ocean data Assimilation and Climate predicTion
(see http://www.ecmwf.int/research/EU_projects/ENACT).

[2]ENSEMBLE-based predictions of climate changes and their impactS
(see http://www.ecmwf.int/research/EU_projects/ENSEMBLES).

rank (implicit) representation of the covariance matrix and thus allows the assimilation method to produce corrections to the background state in a much larger space than that spanned by a limited number of ensemble members. There is also no need for a separate localization procedure since covariance models are constructed to permit only spatially limited covariance functions. The use of ensembles in combination with a variational assimilation scheme is relatively unexplored in ocean data assimilation. The main purpose of this study is to investigate the potential of the ocean ensemble 3D-Var system developed for ENSEMBLES to provide flow-dependent estimates of the background-error *variances*. This study can be viewed as a first step towards making more comprehensive use of the ensemble for calibrating other parameters of the covariance model.

The paper is organized as follows. Section 3 gives a description of the basic components of the data assimilation system. The sensitivity experiments presented in this paper involve different formulations of both the observation-error variances and background-error variances. These formulations, including the background-error variance formulation based on the ensemble method, are described in Section 4. Results from cycled 3D-Var experiments that compare the relative impact of the different variance formulations are presented in Section 5. A summary and conclusions are given in Section 6. Appendix A provides a derivation of the formula used to estimate geographically dependent observation-error variances. Appendix B presents the mathematical basis of the ensemble method used for estimating background-error covariances.

3 The assimilation system

3.1 Ocean model and forcing fields

The ocean model is a global, free-surface configuration of the ocean general circulation model OPA8.2 (Madec *et al.* 1998). The model solves the primitive equations for horizontal currents, $\mathbf{u}_h = (u, v)$, potential temperature, T, salinity, S, and sea surface height (SSH), η. The free-surface formulation is described in Roullet and Madec (2000). The equations are formulated in orthogonal curvilinear z-coordinates and discretized using finite differences on an Arakawa C-grid. The horizontal grid is stretched in the northern hemisphere and contains two poles located on the North American and Asian continents. Outside the equatorial region, the grid mesh is approximately isotropic (Mercator-like) with zonal $\times$ meridional resolution approximately $2° \times 2° \cos \phi$ where ϕ is latitude. Within the equatorial region, the meridional resolution is increased, with the grid size reaching a value of $0.5°$ at the equator. Increased resolution is also used in the Mediterranean Sea ($1° \times 1°$) and Red Sea ($\approx 1° \times 2°$). The number of horizontal grid points is 182×149. The model has 31 levels of which 21 are in the upper 1000 m. The thickness of the levels varies from 10 m within the upper 100 m to 500 m below the 3000 m level. The maximum depth is 5500 m.

Lateral and vertical subgrid scale mixing is parameterized using Laplacian diffusion. Vertical diffusion coefficients for momentum, heat, and salt are computed using a Turbulent Kinetic Energy mixing scheme. Lateral mixing coefficients of momentum, heat and salt are geographically dependent. For heat and salt, the lateral diffusion acts along neutral surfaces and includes an additional tracer advection term following Gent and McWilliams (1990). The model is forced using wind-stress, $\tau = (\tau^x, \tau^y)$, heat flux (Q) and fresh-water (Precipitation minus Evaporation) flux, *PmE*, from ERA40 (Uppala *et al.* 2005). The fresh-water flux from ERA40 is known to be inaccurate. Here the model is forced using bias-corrected ERA40 precipitation from Troccoli and Kållberg (2004).

The ensemble experiments are performed over the 9-yr period 1 January 1993 to 31 December 2001. The experiments are designed to test the impact of using the ensemble to update the background-error variances on each assimilation cycle. A separate set of ensemble experiments covering the 46-yr period 1960-2005 has also been conducted as part of the ENSEMBLES project. The assimilation system used in those experiments is a

close variant of the system used here, the main difference being that there was no attempt to use the ensemble to update the background-error covariance matrix as done in this study. The ENSEMBLES experiments also used a more recent version (EN3) of the quality-controlled *in situ* data-set described in section 3.2 and these data were not perturbed as in this study (see section 4.2). In those experiments, the ocean analysis ensemble was used to provide initial conditions for seasonal and decadal ensemble forecasts. Results from the assimilation experiments conducted in ENSEMBLES are not discussed in this paper, although results from a separate experiment that employs a system similar to the one used in ENSEMBLES is used as a reference for evaluating the impact of the ensemble-generated background-error variances.

The experimental design follows closely the common procedures used in ENSEMBLES and in the earlier project ENACT (Davey *et al.* 2006). The initial conditions on 1 January 1993 were obtained by spinning up the model from rest and temperature and salinity states defined from the Levitus climatology. Climatological ERA40 forcing was used from 1 January 1978 to 31 December 1982, and daily ERA40 forcing was used from 1 January 1983 to 31 December 1992. The model sea surface temperature (SST) field is relaxed to model-gridded SST analysis products. During the spin-up from 1 January 1978 to 31 December 1982, the SST climatology from ERA40 was used, while daily-interpolated SST analyses from Reynolds OI_v2 (Reynolds *et al.* 2002) were used from 1 January 1983 onwards. As in ENACT and ENSEMBLES, a globally uniform relaxation coefficient of $-200\,\mathrm{Wm^{-2}K^{-1}}$ is used, which corresponds to a relaxation time-scale of 12 days for a mixed-layer depth of 50 m. With this choice, the model SST is always close to the "observed" SST. This is an important requirement for seasonal and decadal forecast initialization for which the system has been applied in ENSEMBLES.

Subsurface relaxation to climatology has been applied to control model drift but has been chosen to be rather weak so as not to suppress interannual and decadal variability. A weak global subsurface relaxation to gridded temperature and salinity monthly climatology, smoothed with a 3-month running mean, is applied with a 3-yr timescale at all vertical levels and all grid points, except within 1000 km of coastlines where the relaxation coefficient is reduced smoothly to a value of zero directly at the coastline, and poleward of $60°$ N/S where the relaxation time scale is reduced smoothly from 3 years to 50 days over the latitude band $60°$ N/S to $70°$ N/S. The subsurface relaxation provides a weak relaxation to temperature and salinity climatology in the top ocean model level. For temperature, the relaxation is dominated by the much stronger relaxation to SST described above. For sea surface salinity (SSS), no relaxation is applied other than the weak contribution at the surface from the relaxation to climatology. Imbalances in the fresh-water fluxes cause the globally averaged model SSH field to drift (≈ 0.7 m in 15 yrs). Here the drift has been suppressed by applying a daily correction to the fresh-water fluxes based on the sea-level drift that occurs on the previous day. As a result, the global mean SSH field is very close to zero on any given time step.

3.2 Observations

The assimilation data-set consists of *in situ* temperature and salinity profiles from version EN2_v1 of the EN-ACT/ENSEMBLES quality-controlled data-set (Ingleby and Huddleston 2007). The data are obtained primarily from the World Ocean Database 2001 (WOD01; Conkright *et al.* 2001). After 1990, they are supplemented using data from the World Marine Environmental Laboratory (Johnson *et al.* 2002) and the Global Temperature-Salinity Profile Program. The data-set is essentially composed of bathythermographs (MBTs and XBTs), hydrographic profiles (CTDs and predecessors), moored buoys from the TAO/TRITON and PIRATA arrays, profiling floats and Argo data. Observations determined by the quality control as "*definitely wrong*" or "*probably wrong*" were not assimilated. Additional screening has been done directly in the assimilation system. Observations have been rejected in closed seas, in some semi-enclosed seas (Mediterranean, Red, Baltic and Japan Seas), below 1000 m and poleward of $65°$N/S. The reason for rejecting the data in those regions was based on the inadequacy of the model or assimilation system to use the observational information effectively,

rather than the actual quality of the observations. Vertical thinning of profiles was performed to restrict the number of individual measurements between two model levels to a maximum of five. A background check has also been implemented in the system but was not activated in order to facilitate the comparison of the different experiments by ensuring that exactly the same observations were assimilated in each case.

3.3 Data assimilation method

The data assimilation method is a variant of the multivariate incremental 3D-Var FGAT (First-Guess at Appropriate Time) method described in Weaver *et al.* (2003), Ricci *et al.* (2005) and Weaver *et al.* (2005). A short description is given below to highlight those features of the method that are important in this study.

Let $\mathbf{w} = (T, S)^T$ denote the model vector of temperature T and salinity S, both T and S being understood to be row-vectors defined on the three-dimensional (3D) model grid[3]. Let $\mathbf{w}^b = (T^b, S^b)^T$ be a background estimate of $\mathbf{w}$, and let $\delta\mathbf{w} = (\delta T, \delta S)^T$ be an increment defined such that $\mathbf{w} = \mathbf{w}^b + \delta\mathbf{w}$. Given profile observations of temperature (T_i^o) and salinity (S_i^o) distributed over a time window $t_0 \leq t_i \leq t_N$, 3D-Var FGAT produces an increment $\delta\mathbf{w}^a$ by approximately minimizing the quadratic cost function

$$J[\delta\mathbf{w}] = \frac{1}{2}\delta\mathbf{w}^T \mathbf{B}_{(\mathbf{w})}^{-1} \delta\mathbf{w} + \frac{1}{2}(\mathbf{H}\delta\mathbf{w} - \mathbf{d})^T \mathbf{R}^{-1}(\mathbf{H}\delta\mathbf{w} - \mathbf{d}) \tag{1}$$

where $\mathbf{d} = (..., \mathbf{d}_i^T, ...)^T$, $\mathbf{d}_i = \mathbf{y}_i^o - \mathbf{H}_i\mathbf{w}^b(t_i)$ is the innovation vector, $\mathbf{y}_i^o = (T_i^o, S_i^o)^T$ is the observation vector at measurement time t_i, and $\mathbf{H}_i\mathbf{w}^b(t_i)$ is the background counterpart of the observation vector at t_i. The background state at t_i, $\mathbf{w}^b(t_i) = (T_i^b, S_i^b)^T$, is a subset of the complete model background state vector, $\mathbf{x}^b(t_i) = (T_i^b, S_i^b, \eta_i^b, u_i^b, v_i^b)^T$, that is obtained by integrating the model from t_0 to t_i from the background initial condition $\mathbf{x}^b(t_0)$ available at the start of the window. The model integration can be represented as

$$\mathbf{x}^b(t_i) = M(t_i, t_{i-1})[\mathbf{x}^b(t_{i-1}), \mathbf{f}_i] \tag{2}$$

where $M(t_i, t_{i-1})$ denotes the nonlinear model operator between t_{i-1} and t_i, and $\mathbf{f}_i = (\tau_i^x, \tau_i^y, Q_i, PmE_i)^T$ denotes the vector of external atmospheric surface fluxes used to force the ocean model on the interval t_{i-1} to t_i. These surface fluxes have been made explicit in (2) in order to clarify the description of the ensemble method given in section 4 and appendix B. The matrix $\mathbf{H} = (..., \mathbf{H}_i^T, ...)^T$ in (1) is the observation operator where $\mathbf{H}_i = \mathbf{H}_i^z \mathbf{H}_i^h$ is a 3D interpolation operator at measurement time t_i, which is formulated as the product of a horizontal ($\mathbf{H}_i^h$) and vertical ($\mathbf{H}_i^z$) interpolation operator. Here, $\mathbf{H}_i^z$ is a cubic spline and $\mathbf{H}_i^h$ is a bilinear interpolation operator, specially adapted to irregular grids (such as the global OPA grid) following the remapping technique of Jones (1998).

The matrices $\mathbf{B}_{(\mathbf{w})}$ and $\mathbf{R}$ contain estimates of the background- and observation-error covariances, respectively. Observation errors are assumed to be mutually uncorrelated so that $\mathbf{R} = \mathbf{D}_{(\mathbf{y})} = \mathbf{D}_{(\mathbf{y})}^{1/2}\mathbf{D}_{(\mathbf{y})}^{1/2}$ where $\mathbf{D}_{(\mathbf{y})}^{1/2} = \mathrm{diag}\{\sigma_T^o, \sigma_S^o\}$, σ_T^o and σ_S^o denoting row-vectors that contain estimates of the standard deviations of temperature and salinity observation error. The specification of the observation-error standard deviations is described in section 4. Background errors are assumed to be correlated. The covariance matrix is described by the product of operators

$$\mathbf{B}_{(\mathbf{w})} = \mathbf{K}_{(\mathbf{w})} \mathbf{D}_{(\widehat{\mathbf{w}})}^{1/2} \mathbf{F}_{(\widehat{\mathbf{w}})} \mathbf{F}_{(\widehat{\mathbf{w}})}^T \mathbf{D}_{(\widehat{\mathbf{w}})}^{1/2} \mathbf{K}_{(\mathbf{w})}^T \tag{3}$$

---

[3]Note that a superscript T will be used throughout the paper to indicate the transpose of a matrix or vector. Otherwise the variable T will be used to refer to the model temperature field.

where

$$\mathbf{F}_{(\widehat{\mathbf{w}})} = \begin{pmatrix} \mathbf{F}_{TT} & 0 \\ 0 & \mathbf{F}_{S_U S_U} \end{pmatrix}. \tag{4}$$

$$\mathbf{D}^{1/2}_{(\widehat{\mathbf{w}})} = \begin{pmatrix} \mathbf{D}^{1/2}_T & 0 \\ 0 & \mathbf{D}^{1/2}_{S_U} \end{pmatrix}, \tag{5}$$

and

$$\mathbf{K}_{(\mathbf{w})} = \begin{pmatrix} \mathbf{I} & 0 \\ \mathbf{K}_{ST} & \mathbf{I} \end{pmatrix}. \tag{6}$$

The matrix product $\mathbf{B}_{(\widehat{\mathbf{w}})} = \mathbf{D}^{1/2}_{(\widehat{\mathbf{w}})} \mathbf{F}_{(\widehat{\mathbf{w}})} \mathbf{F}^T_{(\widehat{\mathbf{w}})} \mathbf{D}^{1/2}_{(\widehat{\mathbf{w}})}$ in (3) is block diagonal (univariate) and can be interpreted as a background-error covariance matrix for the vector $\widehat{\mathbf{w}}^b = (T^b, S^b_U)^T$ where S^b_U is an "unbalanced" background salinity variable that is constructed to be approximately uncorrelated with T^b (Weaver *et al.* 2005). The transformation of background errors from $\widehat{\mathbf{w}}$-space to $\mathbf{w}$-space is achieved using the linear balance operator $\mathbf{K}_{(\mathbf{w})}$. Here, $\mathbf{K}_{(\mathbf{w})}$ is formulated so that it leaves T^b errors unchanged but estimates S^b errors as the sum of balanced (S^b_B) and unbalanced (S^b_U) errors where the balanced component is computed directly from T^b errors using the operator $\mathbf{K}_{ST}$. Following Ricci *et al.* (2005), $\mathbf{K}_{ST}$ has been parametrized in terms of the vertical gradients of T^b and S^b so that local salinity changes can be produced in response to local temperature changes to allow approximate preservation of the background water-mass properties. The degree to which the water mass properties are preserved is controlled by the background-error standard deviation matrices $\mathbf{D}^{1/2}_T = \mathrm{diag}\{\sigma^b_T\}$ and $\mathbf{D}^{1/2}_{S_U} = \mathrm{diag}\{\sigma^b_{S_U}\}$ where σ^b_T and $\sigma^b_{S_U}$ are row-vectors containing estimates of the standard deviations of temperature and unbalanced salinity background errors. The main purpose of this study is to explore the potential of an ensemble 3D-Var to provide flow-dependent estimates of these standard deviations.

The block matrices $\mathbf{F}_{TT}$ and $\mathbf{F}_{S_U S_U}$ are 3D univariate smoothing operators, each constructed as the product of a 1D and 2D anisotropic diffusion operator (Weaver and Courtier 2001). The product of $\mathbf{F}_{(\widehat{\mathbf{w}})}$ with its adjoint $\mathbf{F}^T_{(\widehat{\mathbf{w}})}$ is, with appropriate normalization, a 3D correlation operator. The correlation functions implied by the diffusion model are approximately Gaussian. The parameters of the 3D diffusion model are the same as those used for the univariate T correlations in Weaver *et al.* (2003), except for the vertical correlation scales which have been slightly reduced here (they are proportional to the local vertical grid depths). Identical correlation parameters are used for T and S_U. The ensemble 3D-Var could also be used to estimate parameters of the diffusion model although this interesting possibility goes beyond the scope of the current study.

The cost function J is minimized iteratively using a conjugate gradient algorithm (Fisher 1998; Tshimanga *et al.* 2008). To improve the convergence properties of the minimization, a preconditioning transformation $\delta\mathbf{v} = \mathbf{U}^{-1}_{(\mathbf{w})}\delta\mathbf{w}$, where $\mathbf{U}^{-1}_{(\mathbf{w})} = \mathbf{F}^{-1}_{(\widehat{\mathbf{w}})}\mathbf{D}^{-1/2}_{(\widehat{\mathbf{w}})}\mathbf{K}^{-1}_{(\mathbf{w})}$, is employed in (1) resulting in the modified cost function

$$J[\delta\mathbf{v}] = \frac{1}{2}\delta\mathbf{v}^T \delta\mathbf{v} + \frac{1}{2}(\mathbf{H}\mathbf{U}_{(\mathbf{w})}\delta\mathbf{v} - \mathbf{d})^T \mathbf{R}^{-1}(\mathbf{H}\mathbf{U}_{(\mathbf{w})}\delta\mathbf{v} - \mathbf{d}). \tag{7}$$

Forty iterations are performed on each assimilation cycle, which typically results in a 9-order of magnitude reduction of the Euclidean norm of the gradient relative to its initial value. If $\delta\mathbf{v}^a$ denotes the minimizing solution of (7) then the minimizing solution of (1) is determined from $\delta\mathbf{w}^a = \mathbf{U}_{(\mathbf{w})}\delta\mathbf{v}^a$. To produce balanced increments for the other model state variables η, u and v, a more general variable transform is applied to the solution $\delta\mathbf{v}^a$:

$$\delta\mathbf{x}^a = \mathbf{U}\delta\mathbf{v}^a = \mathbf{K}_{(\mathbf{x})}\mathbf{D}^{1/2}_{(\widehat{\mathbf{w}})}\mathbf{F}_{(\widehat{\mathbf{w}})}\delta\mathbf{v}^a \tag{8}$$

where $\delta \mathbf{x}^a = (\delta T^a, \delta S^a, \delta \eta^a, \delta u^a, \delta v^a)^T$ is the analysis increment for the complete model state vector,

$$
\mathbf{K}_{(\mathbf{x})} = \begin{pmatrix} \mathbf{I} & 0 \\ \mathbf{K}_{ST} & \mathbf{I} \\ \mathbf{K}_{\eta T} & \mathbf{K}_{\eta S} \\ \mathbf{K}_{uT} & \mathbf{K}_{uS} \\ \mathbf{K}_{vT} & \mathbf{K}_{vS} \end{pmatrix} \tag{9}
$$

is the full balance operator, and $\mathbf{B} = \mathbf{U}\mathbf{U}^T$ can be interpreted as a reduced-rank error covariance matrix for the complete background state $\mathbf{x}^b$. The operators $\mathbf{K}_{\eta T}$ and $\mathbf{K}_{\eta S}$ in (9) compute a balanced SSH increment, $\delta \eta^a$, by integrating a density increment from a reference depth (1500m) to the surface, where the density increment is computed from δT^a and δS^a using a linearized equation of state. The operators $\mathbf{K}_{uT}$, $\mathbf{K}_{uS}$, $\mathbf{K}_{vT}$ and $\mathbf{K}_{vS}$ compute balanced horizontal velocity increments, δu^a and δv^a, from the geostrophic relation. Near the equator, δv^a is reduced to zero while δu^a is balanced geostrophically using a β-plane approximation (Lagerloef *et al.* 1999). A detailed description of the multivariate balance operator can be found in Weaver *et al.* (2005).

The increment $\delta \mathbf{w}$ and background-error covariance matrix $\mathbf{B}_{(\mathbf{w})}$ are formally defined with respect to $\mathbf{w}^b$. In 3D-Var, $\mathbf{w}^b$ can be chosen from any background state $\mathbf{x}^b(t_i)$ within the window. Following Weaver *et al.* (2003) and Ricci *et al.* (2005), we take $\mathbf{w}^b$ to be the background state at the start of the window. This state is used to define the linearization state in the T-S balance. It is also used in the parameterized formulation of the background-error variances with respect to which the ensemble-generated variances will be compared.

The technique of Incremental Analysis Updates (IAU; Bloom *et al.* 1996) is used to introduce the analysis increment gradually into the ocean model in order to minimize spurious adjustment processes. In this study, IAU is applied over the entire window; i.e., given $\delta \mathbf{x}^a$, the model integration from t_0 to t_N is repeated using a prognostic equation of the form

$$
\mathbf{x}^a(t_i) = M(t_i, t_{i-1})[\mathbf{x}^a(t_{i-1}), \mathbf{f}_i] + F_i \delta \mathbf{x}^a \tag{10}
$$

where $\mathbf{x}^a(t_0) = \mathbf{x}^b(t_0)$, and F_i is a weighting function defined such that $\sum_{i=1}^{N} F_i = 1$. The weighting function has been formulated to give maximum weight in the centre of the window, with the weighting reduced linearly to a small value at the window end-points. Such weighting provides a smooth transition of the analysis trajectory from one assimilation cycle to the next. An assimilation window of $t_N = 10$ days has been used for the experiments in this study. The procedure for cycling the 3D-Var is represented schematically in Fig. 1.

4 Specification of the observation- and background-error variances

4.1 Observation-error variance matrix: $\mathbf{D}_{(\mathbf{y})}$

Two formulations of the observation-error variance matrix have been tested in this study. The first formulation, denoted $\mathbf{D}_{(\mathbf{y})}^{(1)}$, is based on a simple analytical function that depends, except near coastlines, on depth only. The function has been constructed to provide an approximate fit to the vertical profiles of globally averaged temperature and salinity observation-error standard deviations (σ^o) estimated by Ingleby and Huddleston (2007) (see their Table 3). For temperature, σ^o is maximum at 75 m depth where it has a value of 1°C compared to 0.75°C at the surface and its minimum value of 0.07°C in the deep ocean. For salinity, σ^o decreases exponentially with depth from 0.18 psu at the surface to a minimum value of 0.02 psu in the deep ocean. Near coastlines, where our coarse resolution model is a poor representation of the real ocean, the σ^o profiles have been inflated. The inflation factor has been set to a value of two directly at the coastline and decreases smoothly to a value of one beyond 300 km from the coastline.

$$\mathbf{x}_c^a(t_N) = \mathbf{x}_{c+1}^b(t_0)$$

$$\mathbf{x}_{c-1}^a(t_N) = \mathbf{x}_c^b(t_0)$$

t_0 cycle $c-1$ t_N t_0 cycle c t_N time
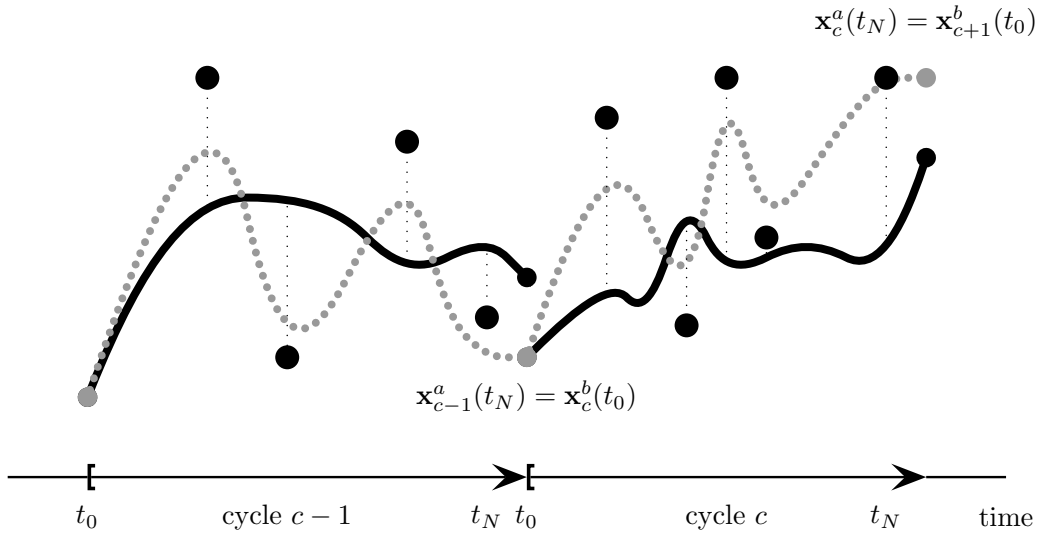
Figure 1: Schematic illustration of the procedure used to cycle 3D-Var. On each cycle c, the model is integrated from t_0 to t_N starting from a background initial condition $\mathbf{x}_c^b(t_0)$ (grey dots) to produce the background trajectory $\mathbf{x}_c^b(t_i)$ (black solid curve). The difference between the observations $\mathbf{y}_{c,i}^o$ (black dots) and their background counterpart $(\mathbf{H}_{c,i}\mathbf{x}_c^b(t_i))$ is computed (represented by the vertical thin dotted lines) for use in the 3D-Var FGAT minimization. After minimization, the model integration is repeated from the same initial condition $(\mathbf{x}_c^b(t_0))$ but with the analysis increment applied using IAU. This produces the analysis trajectory $\mathbf{x}_c^a(t_i)$ (grey dashed curve). The updated model state $\mathbf{x}_c^a(t_N)$ at the end of cycle c is then used as the background initial condition for the next cycle $c+1$ (grey dots).

The second formulation, denoted $\mathbf{D}_{(\mathbf{y})}^{(2)}$, employs geographically-dependent temperature and salinity σ^o that have been estimated using a statistical method originally proposed by Fu *et al.* (1993). The method has been widely used in ocean data assimilation (Fukumori 2000; Menemenlis and Chechelnitsky 2000; Leeuwenburgh 2007). Given a vector $\mathbf{w}^c = (T^c, S^c)^T$ of temperature and salinity fields computed from a model integration without data assimilation (the control run in this study), the Fu *et al.* method estimates the observation-error variances from the covariance between co-located observation and observation-minus-control anomalies:

$$\mathbf{D}_{(\mathbf{y})}^{(2)} = \mathrm{diag}\left\{ \overline{\mathbf{y}_i^{o\prime}\left(\mathbf{y}_i^{o\prime} - \mathbf{H}_i\mathbf{w}_i^{c\prime}\right)^T} \right\} \tag{11}$$

where the overbar indicates an appropriate time and spatial average, and the prime indicates anomaly with respect to this average. A derivation of (11) is given in appendix A. In particular, it involves a crucial assumption that the true state be uncorrelated with the errors in both the observations and the control state. While this assumption may be difficult to justify theoretically, it may not be particularly severe when viewed in combination with other practical assumptions made in quasi-operational data assimilation systems such as ours.

The variance computation has been performed using all *in situ* data between January 1962 and December 2002 contained in the ENSEMBLES data-set (see section 3.2). Estimates have been made at each model grid point by averaging covariances within that model grid cell. In some regions, such as the deep ocean and Southern Hemisphere, the σ^o are grossly underestimated due to the sparseness of the data. To avoid this problem, the Ingleby and Huddleston variances were imposed as minimum values. The σ^o were then smoothed in each level by applying a local two grid-point Shapiro filter. Finally, the model-gridded σ^o were interpolated to the observation locations using the observation operator, and inflated near coastlines as in $\mathbf{D}_{(\mathbf{y})}^{(1)}$. Both $\mathbf{D}_{(\mathbf{y})}^{(1)}$ and $\mathbf{D}_{(\mathbf{y})}^{(2)}$ provide estimates of only the stationary component of σ^o. No attempt was made to estimate a time varying component of σ^o due to the sparseness of the data.

The global profiles of σ^o computed from (11) (figure not shown) have similar characteristics to those of Ingleby and Huddleston (2007) although are noticeably larger above 1500 m. For temperature, the largest difference

between the two estimates is $0.3°C$ and occurs near the maximum value of σ^o at 75 m. For salinity, the largest difference is 0.05 psu and occurs at the surface. The geographical distribution of σ^o is illustrated in Fig. 2 for temperature at depths 50 m and 500 m. These are the estimates of σ^o computed directly from (11), before additional filtering and processing to fill in data-sparse regions. The fields are roughly similar to those estimated by Leeuwenburgh (2007), exhibiting largest σ^o (up to $3°C$) in regions characterized by strong internal variability. At both depths, σ^o is large in western boundary current regions, in particular the Gulf Stream, Kuroshio, Agulhas and Malvinas Current regions, where there is significant mesoscale activity that our coarse resolution model cannot resolve. The large values of σ^o in these regions thus probably reflect a large representativeness error component in the observation error. At 50 m (Fig. 2a), σ^o is also large in the eastern parts of the tropical Pacific and Atlantic Oceans where this depth coincides with the thermocline. Between 50-200 m (not shown), the large patterns of σ^o near the equator in the tropical Pacific migrate toward the central and western parts of the basin, commensurate with the deepening of the thermocline from east to west. At 500 m (Fig. 2b), the σ^o remain large only in mid-latitude boundary current regions.

(a) σ_T^o at 50 m   (b) σ_T^o at 500 m
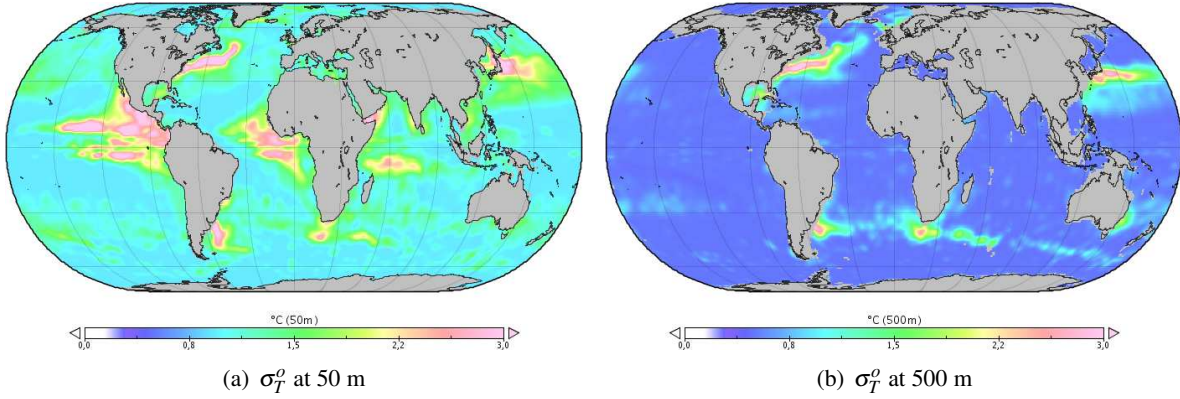
Figure 2: Model-gridded standard deviations of observation error (σ^o) for temperature at a) 50 m and b) 500 m, estimated using the Fu et al. method.

4.2   Background-error variance matrix: $\mathbf{D}_{(\widehat{\mathbf{w}})}$

Two flow-dependent formulations of the background-error variance matrix have been tested in this study. The first formulation, denoted $\mathbf{D}_{(\widehat{\mathbf{w}})}^{(1)}$, is based on an empirical parameterization. For temperature, the background-error standard-error deviations (σ^b) are parameterized in terms of the vertical gradient of the background temperature field so that large σ^b are concentrated at the level of the thermocline where thermal variability is greatest. Weaver *et al.* (2003) illustrate how this simple variance parameterization can capture some of the dynamical effects implicit in 4D-Var. A similar parameterization is used in the operational ocean data assimilation systems at the National Centers for Environmental Prediction (Behringer *et al.* 1998) and ECMWF (Balmaseda *et al.* 2008). The parameterization is described by the equation

$$\sigma_T^b = \begin{cases} \max\left(\tilde{\sigma}_T^b, \, \sigma_T^{ml}\right) & \text{in the mixed layer,} \\ \max\left(\tilde{\sigma}_T^b, \, \sigma_T^{do}\right) & \text{below the mixed layer,} \end{cases} \tag{12}$$

where

$$\tilde{\sigma}_T^b = \min\left(\left|(\partial T/\partial z|_{T=T^b}) \, \delta z\right|, \, \sigma_T^{max}\right), \tag{13}$$

σ_T^{max} being the maximum-allowed value of σ_T^b, δz a vertical scale, and σ_T^{ml} and σ_T^{do} lower bounds in the mixed layer and deep ocean, respectively. In this study, as in Weaver *et al.* (2005), $\sigma_T^{max} = 1.5°C$, $\delta z = 10$ m, $\sigma_T^{ml} =$

0.5°C, and $\sigma_T^{do} = 0.07$°C. Finally, the σ_T^b was smoothed in each model level using a diffusion (Gaussian) filter with geographically dependent length scales identical to those specified in the horizontal correlation operator.

For unbalanced salinity, σ^b is defined somewhat ad hocly according to the equation

$$\sigma_{S_U}^b = \begin{cases} \sigma_{S_U}^{max} & \text{if } z > z_{max} \\ \sigma_{S_U}^{max} \alpha(z) & \text{if } z \leq z_{max} \end{cases} \tag{14}$$

where $\sigma_{S_U}^{max} = 0.25$ psu, z_{max} is the depth of the maximum of $|(\partial S/\partial T|_{T=T^b})| \equiv |(\partial S/\partial z|_{S=S^b})(\partial z/\partial T|_{T=T^b})|$, and

$$\alpha(z) = 0.1 + 0.45 \times \{1 - \tanh(2\ln(z/z_{max}))\} \tag{15}$$

is a weighting coefficient that decreases with depth. The above parameterization thus defines the largest $\sigma_{S_U}^b$ between the surface and the level of maximum $S(T)$ gradients. This is especially important in the mixed layer since there salinity is described primarily by its unbalanced component (Ricci *et al.* 2005). The empirical formulation of σ^b will serve as a reference for evaluating the ensemble-generated σ^b described below.

The second formulation, denoted $\mathbf{D}_{(\widehat{\mathbf{w}})}^{(2)}$, is derived from an ensemble method which is similar to the method employed in the meteorological variational data assimilation studies of Fisher (2003), Žagar *et al.* (2005) and Berre *et al.* (2006). Appendix B provides the mathematical basis of the method. There it is shown how a perturbed cycled analysis/forecast system leads to identical linearized evolution equations for the analysis and forecast state perturbations as those for the true errors. Consequently, if the perturbations to the input parameters are constructed to have covariance matrices equal to those of the true errors then, to first order, the evolving analysis/forecast perturbations of the ensemble will also have covariance matrices equal to those of the true errors.

The method for cycling the ensemble analysis/forecast system is summarized schematically in Fig. 3. Assuming that the different ensemble members are uncorrelated then, as discussed in appendix B (see equation (58)), $\mathbf{D}_{(\widehat{\mathbf{w}})}$ can be estimated from the difference between background states $\mathbf{w}_l^b(t_0)$ of successive ensemble members, $l = 0, \dots, L$:

$$\mathbf{D}_{(\widehat{\mathbf{w}})}^{(2)} = \text{diag}\left\{ \frac{1}{2(L-1)} \sum_{l=0}^{L} \left[\mathbf{K}_{(\mathbf{w})}^{-1} \left(\mathbf{w}_l^b(t_0) - \mathbf{w}_{l+1}^b(t_0) \right) \right] \left[\mathbf{K}_{(\mathbf{w})}^{-1} \left(\mathbf{w}_l^b(t_0) - \mathbf{w}_{l+1}^b(t_0) \right) \right]^T \right\} \tag{16}$$

where

$$\mathbf{K}_{(\mathbf{w})}^{-1} = \begin{pmatrix} \mathbf{I} & 0 \\ -\mathbf{K}_{ST} & \mathbf{I} \end{pmatrix} \tag{17}$$

and $\mathbf{w}_{L+1}^b(t_0) = \mathbf{w}_0^b(t_0)$. Equation (16) can be related to (58) by noting that $\mathbf{w}_l^b(t_0) = \mathbf{w}_{l,c}^b(t_0) = \mathbf{w}_{l,c-1}^a(t_N)$ where c is the cycle number. Equation (17) is the inverse of the balance operator (6) and is needed in order to estimate σ^b for $\widehat{\mathbf{w}}$ as required by the covariance model (3).

Key to the design of the ensemble system is the construction of the perturbations for the system input parameters. In appendix B, the ensemble method is developed while considering a general set of input parameters consisting of the external surface forcing fields, initial state, observations, and model-error source terms. Ideally, the perturbations should be chosen to sample the true statistical uncertainty in these parameters. The true error statistics of the input parameters are unknown and must be approximated in practice. In this study, the perturbations $\tilde{\varepsilon}_{l,i}^f$, $l = 1, \dots, L$, to the surface fields (wind-stress, heat flux, PmE) are defined from differences between different analysis products (see below). The perturbations $\tilde{\varepsilon}_{l,i}^o$ to the observations are drawn from a Gaussian distribution with covariance matrix equal to the diagonal $\mathbf{R}$-matrix used in the assimilation system.
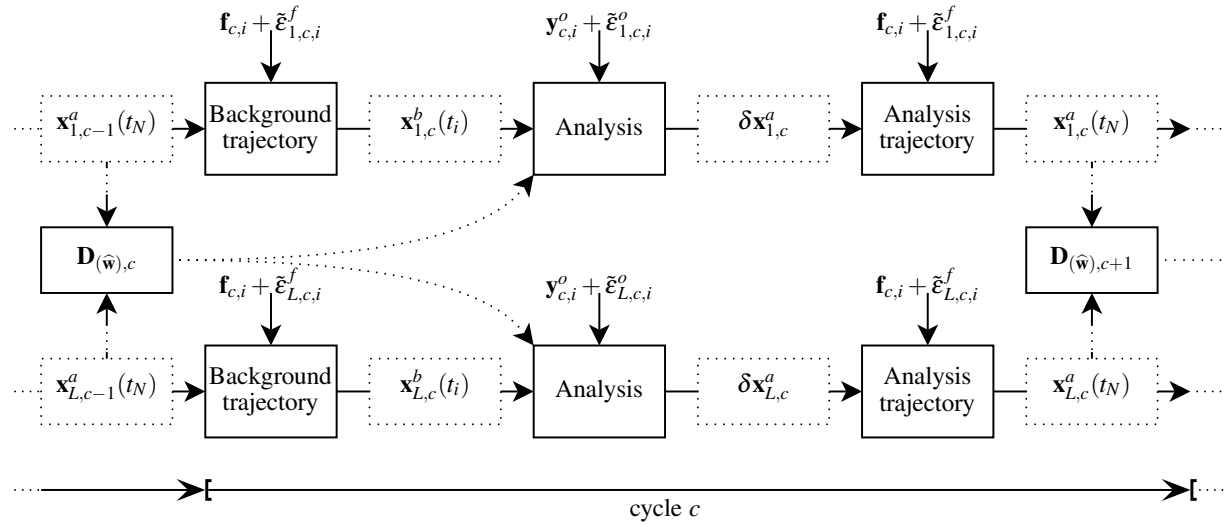
Figure 3: Schematic illustration of the ensemble 3D-Var system. The ensemble of analysis states $\mathbf{x}_{l,c-1}^a(t_N)$, $l = 1, \ldots L$, at the end of cycle $c-1$ are used to initialize the background trajectories of each ensemble member on the next cycle c. The background trajectory of each member l is produced by integrating the model with a perturbed set of forcing fields (wind-stress, heat flux, PmE), $\mathbf{f}_{c,i} + \tilde{\varepsilon}_{l,c,i}^f$, from the initial condition $\mathbf{x}_{l,c}^b(t_0) = \mathbf{x}_{l,c-1}^a(t_N)$. Each background trajectory is compared with a set of perturbed observations $\mathbf{y}_{c,i}^o + \tilde{\varepsilon}_{l,c,i}^o$ to produce an innovation vector for each member l. A 3D-Var (FGAT) analysis is then performed for each ensemble member using the appropriate innovation vector and a background-error variance matrix $\mathbf{D}_{(\hat{\mathbf{w}}),c}$ that has been estimated from the ensemble of background initial states $\mathbf{x}_{l,c}^b(t_0)$. The unperturbed member ($l = 0$), which is not displayed, is also used to compute $\mathbf{D}_{(\hat{\mathbf{w}}),c}$ (see equation (58)). The resulting analysis increment is then used to produce an analysis state trajectory as described in Fig. 1.

The background initial state perturbations $\tilde{\varepsilon}_l^b(t_0) = \tilde{\varepsilon}_{l,c}^b(t_0)$ are set to zero on the first cycle ($c = 1$). On subsequent cycles, these perturbations are defined implicitly as the difference between the perturbed and unperturbed background states ($\tilde{\varepsilon}_l^b(t_0) = \mathbf{x}_{l,c}^b(t_0) - \mathbf{x}_{0,c}^b(t_0)$). Perturbations associated with model error $\tilde{\varepsilon}_{l,i}^q$ are neglected altogether in this study.

The perturbations to the surface forcing fields have been derived by ECMWF where they are used to produce ensembles of initial conditions for operational seasonal forecasting (Balmaseda *et al.* 2008). They have also been used by various groups for ocean analysis production in the ENSEMBLES project. For wind-stress, the perturbations are computed from differences between monthly mean anomalies from the ERA40 and NCEP/NCAR reanalysis products. Perturbations to the fresh-water flux have been introduced in the precipitation field only, and are computed from differences between monthly mean anomalies of bias-corrected ERA40 and NCEP/NCAR precipitation fields. To define the forcing perturbations for a given date and a given ensemble member, the perturbations are chosen randomly among the various difference fields that have the same calendar month (a sample of 44). Finally, daily perturbations of wind-stress and fresh-water flux are computed from the monthly fields using linear interpolation.

Perturbations of SST are used as a proxy for perturbations in heat flux, and are derived from differences between daily anomalies from different Reynolds products (2DVAR and OIv2). The SST perturbations for a given date and ensemble member are constructed following the same random-selection procedure used for the wind-stress and fresh-water flux perturbations. The procedure leads to a set of daily SST perturbations that, for a given member, are uncorrelated from one day to the next. To remove the temporal discontinuity, the daily SST perturbations have been smoothed in time using a two-pass recursive filter which is equivalent to correlating the perturbations with a second-order auto-regressive function (Purser *et al.* 2003). A filtering time-scale of 7 days was used. The perturbations were then rescaled to ensure that the globally averaged standard deviation was the same before and after filtering.

Four sets of surface forcing field perturbations were generated using the procedure above. Eight perturbed forcing fields were then produced by adding and subtracting the four forcing perturbations from the unperturbed fields. A different set of randomly perturbed observations were defined for each of the eight branches involving different forcing fields. The eight perturbed branches plus the unperturbed branch give a 9-member ensemble. Variances computed from this relatively small ensemble size were too noisy to be used directly in the assimilation system. In order to increase the sample size, a sliding window was used to include the ensemble of background states from the previous 9 cycles (90 days) in the computation of the variances for the current cycle. This effectively increased the ensemble size to 81. Assuming Gaussian statistics, the standard error in the estimated standard deviation for an ensemble size L is $1/\sqrt{2L}$ (e.g., see Barlow (1989), p.89). Thus, with $L = 81$, the error is 8% compared to 24% with $L = 9$. A 17-member ensemble with four perturbed observation branches for each perturbed forcing branch was also tested (with and without a 9-cycle sliding window) but did not lead to noticeable improvements over the 9-member ensemble (with 9-cycle sliding window) to justify the extra computational cost. The use of a sliding window represents a compromise between the desire to have truly flow-dependent background-error variances, on the one hand, and to reduce sampling error, on the other. In particular, with the 90-day window used here, background-error variations on intraseasonal time-scales are filtered out and those on seasonal time-scales are strongly damped. Maximum values of $3.0°C$ and 0.8 psu and minimum values of $0.07°C$ and 0.01 psu were used as bounds for the ensemble σ^b.

5 Results

Four experiments were performed over the period 1993-2000 to test the sensitivity of the analyses to the different background- and observation-error variance formulations presented in the previous section. Experiment B1R1 uses the parameterized σ^b and simplified σ^o. This experiment and the control (CTL) are our reference experiments. Experiment B1R2 uses the parameterized σ^b and the σ^o estimated using the Fu *et al.* method. The reanalysis experiments conducted by CERFACS in ENACT (Davey *et al.*, 2006) and ENSEMBLES used the variance specifications in B1R1 and B1R2, respectively. Experiment B2R2 uses the ensemble σ^b, and the σ^o from the Fu *et al.* method. The parameterized σ^b were used to initialize B2R2 on 1 January 1993 but were then replaced with the ensemble σ^b 180 days after cycling. All time-averaged statistics presented in this section exclude the first year of the experiments. The different ensemble members of B2R2 produced statistically similar results. Unless stated otherwise, results from B2R2 will be presented from the unperturbed member. The assimilation experiments are summarized in Table 1.

Our objective in this paper is to provide an overall assessment of the relative performance of the different experiments, so we focus mainly on global diagnostics in this section. An exception is in section 5.6 where results involving comparisons with independent data are presented for the northwest Atlantic and tropical Pacific regions.

Experiment name	$\mathbf{D}^{(1)}_{(\widehat{\mathbf{w}})}$	$\mathbf{D}^{(2)}_{(\widehat{\mathbf{w}})}$	$\mathbf{D}^{(1)}_{(\mathbf{y})}$	$\mathbf{D}^{(2)}_{(\mathbf{y})}$
B1R1	X		X	
B1R2	X			X
B2R2		X		X

Table 1: Summary of the background- and observation-error variance matrix formulations used in the different experiments. The matrices $\mathbf{D}^{(1)}_{(\widehat{\mathbf{w}})}$ and $\mathbf{D}^{(2)}_{(\widehat{\mathbf{w}})}$ contain the parameterized and ensemble-estimated background-error variances, respectively. The matrices $\mathbf{D}^{(1)}_{(\mathbf{y})}$ and $\mathbf{D}^{(2)}_{(\mathbf{y})}$ contain the simplified and Fu et al.*-estimated observation-error variances, respectively.*

5.1 Geographical distribution of σ^b

Figure 4 shows an example of the parameterized estimates of the σ_T^b from B1R2 (upper panels) and the corresponding ensemble estimates of the σ_T^b from B2R2 (lower panels) obtained near the end of the assimilation period (27 August 1999). The fields are displayed at depths of 50 m (left panels) and 500 m (right panels). The spatial structures of the two estimates of σ_T^b are generally very different. Large σ_T^b in the parameterized estimates occur in areas where the background temperature profile is strongly stratified. The large patterns at 50 m in the Northern Hemisphere reflect the increased stratification of the seasonal thermocline in the boreal summer (Fig. 4a). The parameterized estimates are also noticeably smoother than the ensemble estimates, largely as a result of the spatial filtering that is applied to the former. The ensemble σ_T^b at both depths are characterized by large estimates in the tropical Pacific, tropical Atlantic, and northwest Atlantic. The upper ocean thermal fields in the tropical Pacific and northwest Atlantic are relatively well observed and strongly influenced by the surface forcing so there the observation and forcing perturbations are expected to have a large impact. In those regions, the ensemble σ_T^b can be slightly larger than the parameterized σ_T^b (values reach 1.9°C at a few isolated points). On the other hand, the parameterized σ_T^b, by construction, never exceed 1.5°C (note that the maximum values in all panels have been cut off at 1.2°C). At both depths, there are also large areas of the ocean, particularly in the Southern Hemisphere, where the ensemble σ_T^b are small. Furthermore, in contrast to the parameterized σ_T^b, the ensemble σ_T^b do not display any obvious dependence on the seasonal thermocline, possibly due to the 90-day sampling window used to construct them.

The large values of the ensemble σ_T^b in the northwest Atlantic, particularly at 500 m, are in sharp contrast to the parameterized σ_T^b which have no discernible signal there due to the weak stratification in the background temperature profile at this depth. Large σ^b will act to reduce the weight of the background relative to the data. In B2R2, the large σ_T^b in the northwest Atlantic are largely compensated by large σ_T^o estimates (Fig. 2). This was vital in B2R2 to avoid overfitting the data in this region which could otherwise lead to numerical instabilities. Indeed, this was the case when the ensemble σ^b were initially used in combination with the simplified σ^o estimates, and subsequently led us to implement the Fu *et al.* method.

5.2 Vertical profiles of σ^b and σ^o

The vertical profiles of the prescribed σ^b and σ^o are illustrated in this section for the different experiments. For consistency with the observation-space diagnostics presented later in this paper, both σ^b and σ^o have been evaluated by first computing the variances $(\sigma^b)^2$ and $(\sigma^o)^2$ at observation points, then averaging the variances in space and time, and finally taking the square root to obtain the standard deviations. Here, the spatial averaging is performed over the global region and within the vertical model grid cells, and the time averaging is performed over the 1994-2000 period. The specified background-error variances $(\sigma^b)^2$ at observation points correspond to the diagonal elements of $\mathbf{HB_{(w)}H}^T$. To compute the diagonal of $\mathbf{HB_{(w)}H}^T$ requires a specific algorithm since this matrix is only available in operator form in our system. The diagonal elements can be estimated at a reasonable cost using a randomization algorithm (Andersson *et al.* 2000). Specifically, given an ensemble of Gaussian random vectors $\mathbf{v}_m$, $m = 1, \ldots, M$, drawn from a population with zero mean and unit variance ($E[\mathbf{v}_m] = 0$ and $E[\mathbf{v}_m\mathbf{v}_m^T] = \mathbf{I}$ where $E[\cdot]$ is the expectation operator) then

$$\mathbf{HB_{(w)}H}^T \approx \frac{1}{M-1} \sum_{m=1}^{M} \left(\mathbf{HU_{(w)}v}_m\right) \left(\mathbf{HU_{(w)}v}_m\right)^T \qquad (18)$$

where $\mathbf{B_{(w)}} = \mathbf{U_{(w)}U_{(w)}^T}$ (see section 3). On each cycle, (18) was used with an ensemble of $M = 100$ random vectors to produce an estimate of σ^b at observation points, with an estimated error of approximately 7%.

(a) Parameterized σ_T^b at 50 m

(b) Parameterized σ_T^b at 500 m

(c) Ensemble σ_T^b at 50 m

(d) Ensemble σ_T^b at 500 m
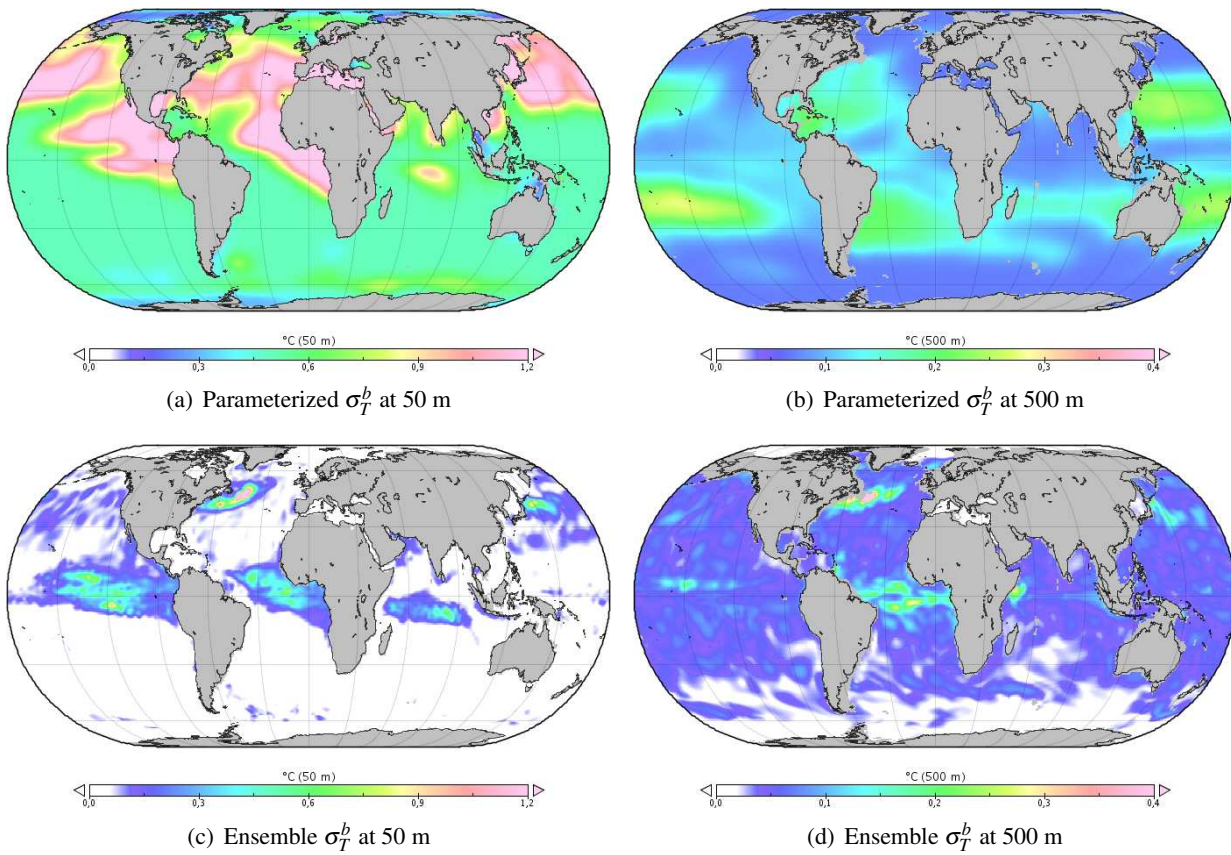
Figure 4: The temperature σ^b field on 27 August 1999 from experiment B1R2 (upper panels) and experiment B2R2 (lower panels) at 50 m (left panels) and 500 m (right panels). For B2R2, the σ^b field is computed from analysis-state samples extending nine 10-day cycles into the past (a total of 81 samples). The maximum value in the colour bar has been set to 1.2°C in the left panels and to 0.4°C in the right panels (light pink shaded areas), but can reach up to 1.5°C, 1.9°C and 0.6°C in the upper left, lower left and lower right panels, respectively.

Figure 5 shows vertical profiles of the specified σ^o and σ^b for temperature (left panels) and salinity (right panels). At all depths, but especially in the upper 200 m, the ensemble-estimated σ^b of B2R2 are smaller than the parameterized σ^b of B1R1 and B1R2, while the Fu *et al.*-estimated σ^o of B1R2 and B2R2 are larger than the simplified σ^o of B1R1. The ratio $(\sigma^b)^2[(\sigma^b)^2 + (\sigma^o)^2]^{-1}$, displayed in the lower panels, roughly indicates the average weight given to an innovation at a particular depth in determining the analysis increment (see equations (43) and (44)). For B2R2, the weights are noticeably smaller and more uniform with depth compared to those from B1R1 and B1R2. As a result, the analysis on each cycle of B2R2 will tend to remain closer to the background state than it will in either B1R1 or B1R2 which will tend to pull it more to the observations, especially in the upper 200 m.

5.3 Assimilation statistics

The innovation vector, $\mathbf{d} = \mathbf{y}^o - \mathbf{Hw}^b$, and analysis increment, $\delta\mathbf{w}^a$, provide valuable information for assessing the statistical performance and internal consistency of the assimilation system (Desroziers *et al.* 2005). In this section, we examine mean statistics of $\mathbf{d}$ and the analysis residual, $\mathbf{r} = \mathbf{d} - \mathbf{H}\delta\mathbf{w}^a$, where these vectors, with the time index omitted, are understood to contain the innovation vectors and analysis residuals from all cycles in the 1994-2000 period. The analysis residual $\mathbf{r}$ (simply called the *residual* in what follows) corresponds to the value, at the minimum, of the difference field in the observation term of the 3D-Var FGAT cost function (1). Whereas $\mathbf{r}$ quantifies the fit to the data achieved by the assimilation method, it does not represent the actual fit to the data achieved after correcting the model integration using IAU, which is given by $\tilde{\mathbf{r}} = \mathbf{y}^o - \mathbf{Hw}^a$. Indeed, by construction, the IAU procedure does not produce a close fit to the data near the beginning of each cycle so that, in general, $\|\tilde{\mathbf{r}}\| > \|\mathbf{r}\|$.

Figure 6 shows the vertical profiles of the time-mean of the globally averaged residual (upper panels) and innovation vector (lower panels) for temperature (left panels) and salinity (right panels). A non-zero mean in the innovations and residuals is an indication of bias (systematic error) in the system (Dee and Todling 2000; Balmaseda *et al.* 2007). In CTL there is a large negative bias above 200 m in both the temperature and salinity innovations (Figs. 6c and d), where the model without data assimilation is, on average, too warm (up to 0.7°C) and too salty (up to 0.6 psu) compared to observations. The mean temperature innovations change sign near 250 m suggesting that the model is biased cold below this level. The mean salinity innovations are very small below 200 m, possibly as a result of the subsurface relaxation to climatology. The mean innovations are reduced substantially, especially for salinity, in all assimilation experiments. The mean residuals are slightly smaller than the mean innovations. They are smallest for B1R1 (grey shade) which is understandable since the σ^o in B1R1 are smaller than those used in B1R2 and B2R2, so that the assimilation method will tend to give more weight to the observations in B1R1 than in B1R2 and B2R2. In all experiments, the remaining biases, while much smaller than in CTL, are still significant, the largest being at the surface in B2R2 where the maximum innovation biases are approximately -0.3°C and -0.11 psu.

Figure 7 shows vertical profiles of the standard deviation (sd) of the residual and innovation vectors:

$$\text{sd}(\mathbf{z}) = \sqrt{\overline{(\mathbf{z} - \overline{\mathbf{z}})^2}} \tag{19}$$

where $\mathbf{z} = \mathbf{d}$, $\mathbf{r}$ or $\tilde{\mathbf{r}}$, and the overbar indicates spatial average over the globe and within vertical model grid cells, and temporal average over the 1994-2000 period. The standard deviation indicates how well the model fits the observed temporal and spatial variability. The CTL exhibits large errors in both temperature and salinity, particularly in the upper 150 m where signals associated with seasonal and interannual variability are largest. Maximum differences are 2.25°C for temperature and 1.65 psu for salinity. Relative to CTL, all assimilation experiments improve the fit to the observed temperature and salinity variability at all depths. This is true on the global average (Fig. 7) although in the equatorial Pacific (figure not shown) the salinity variability below
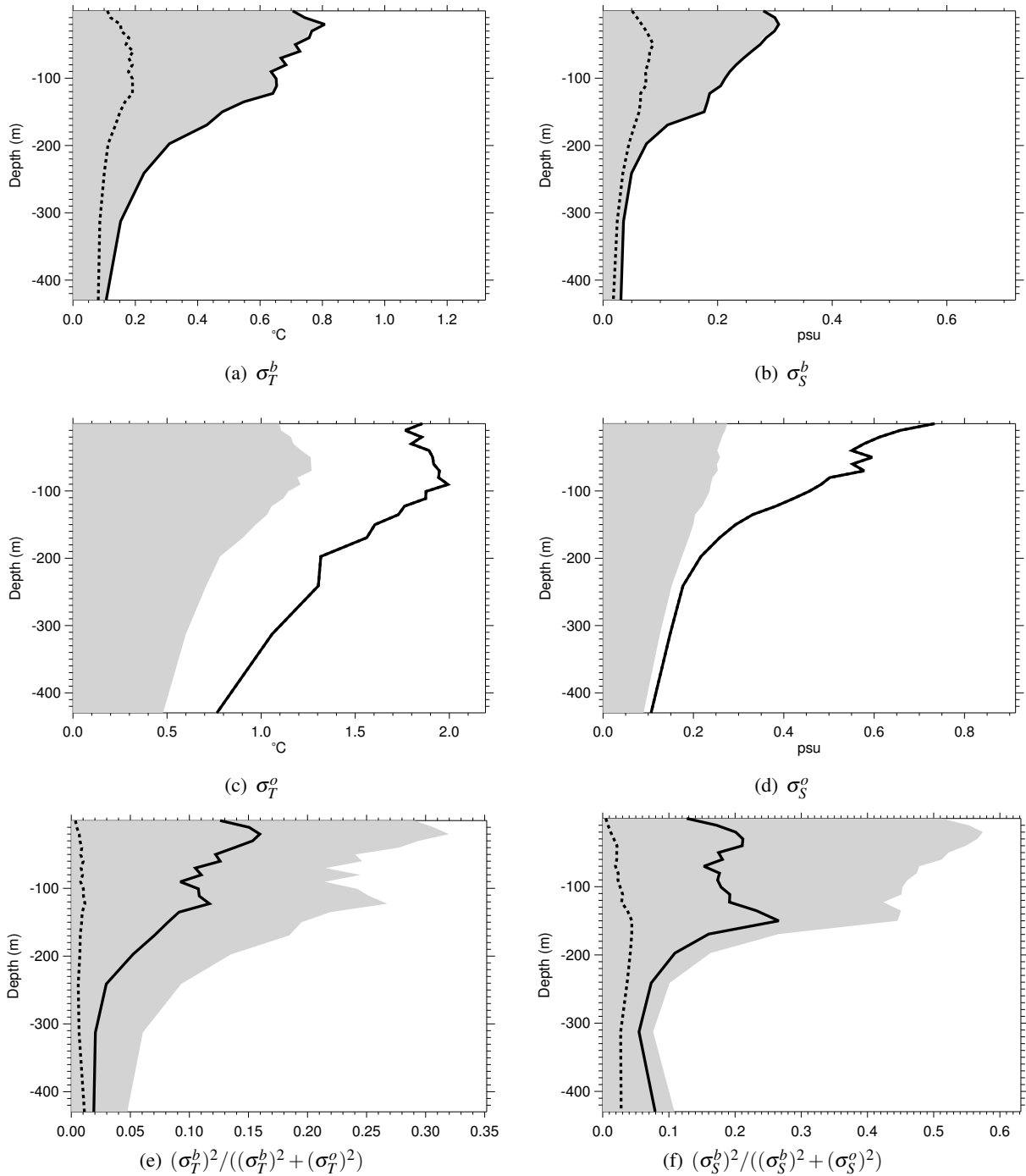
Figure 5: Vertical profiles of σ^b (upper panels) and σ^o (middle panels) for temperature (left panels) and salinity (right panels) in B1R1 (grey shaded areas), B1R2 (solid curves) and B2R2 (dashed curves). The ratio $(\sigma^b)^2[(\sigma^b)^2 + (\sigma^o)^2]^{-1}$ is displayed in the lower panels. The solid and dashed curves coincide in the upper panels. Both $(\sigma^b)^2$ and $(\sigma^o)^2$ have been computed at observation points, temporally averaged over the 1994-2000 period, and spatially averaged over the global region and within vertical model grid cells.

(a) Temperature residual

(b) Salinity residual

(c) Temperature innovation

(d) Salinity innovation
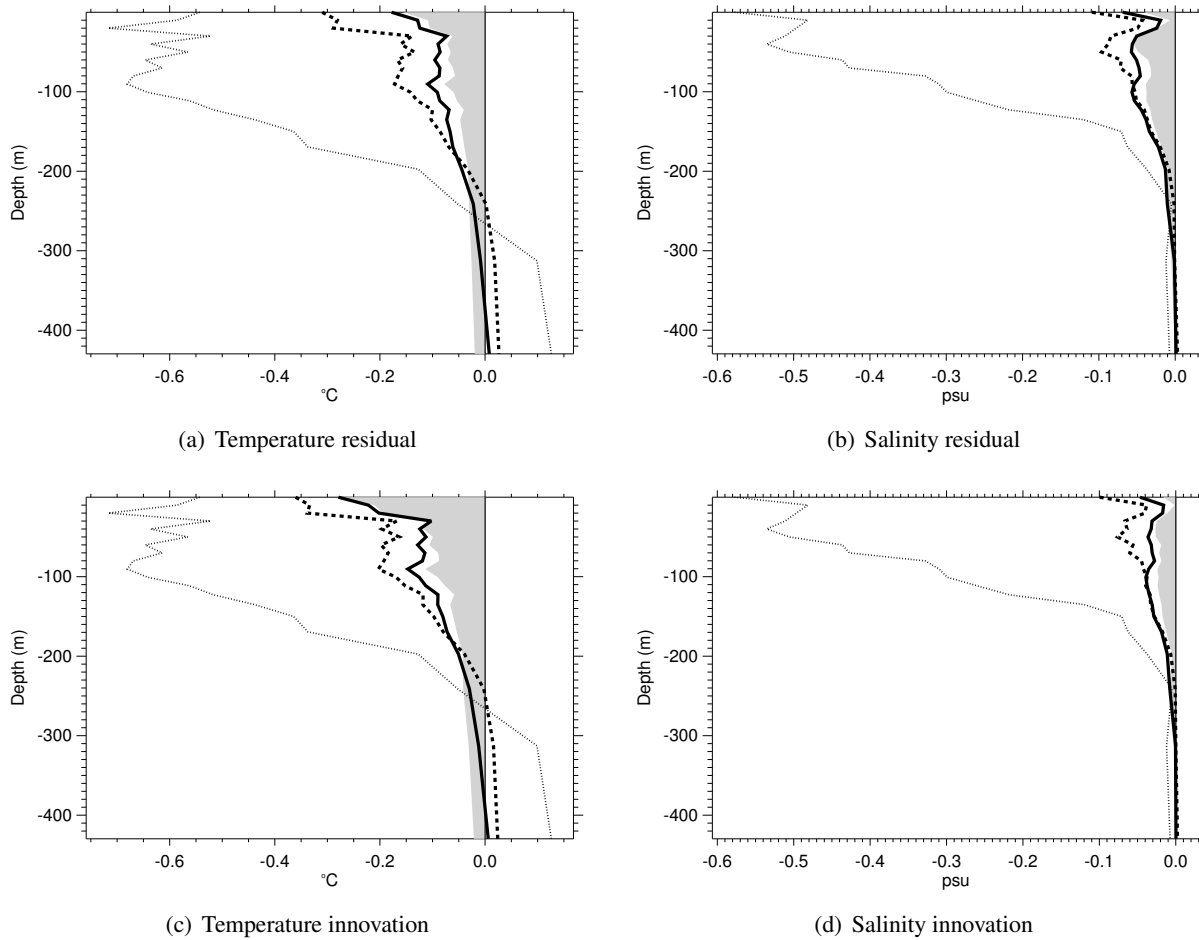
Figure 6: Vertical profiles of the 1994-2000 time-mean of the globally averaged innovations ($\mathbf{d} = \mathbf{y}^o - \mathbf{H}\mathbf{w}^b$; lower panels) and analysis residuals ($\mathbf{r} = \mathbf{d} - \mathbf{H}\delta\mathbf{w}^a$; upper panels) for temperature (left panels) and salinity (right panels) for CTL (thin dotted curves), B1R1 (grey shaded areas), B1R2 (solid curves) and B2R2 (dashed curves). Values have been averaged onto model levels. For CTL the innovation and residual are identical ($\delta\mathbf{w}^a = 0$).

(a) Temperature residual

(b) Salinity residual

(c) Temperature innovation

(d) Salinity innovation
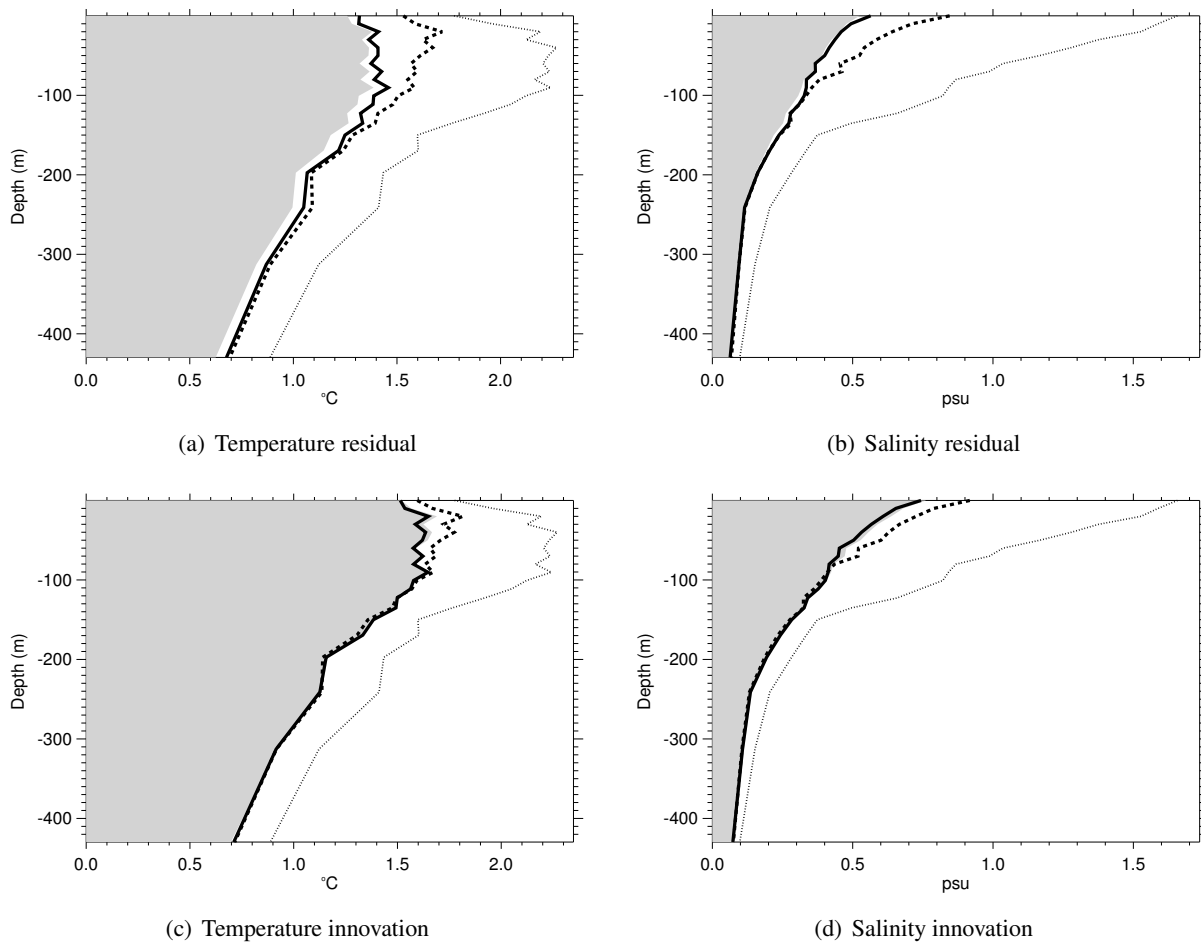
Figure 7: Same as Fig. 6 but the standard deviation of the innovations (sd($\mathbf{d}$)) and analysis residuals (sd($\mathbf{r}$)) as defined by (19).

50 m was found to be slightly degraded in B1R1 and B1R2, but not in B2R2, which points to a deficiency in the parameterized estimates of σ_S^b. Differences between B1R1 and B1R2 are small (shaded and solid curves). B1R1 displays slightly smaller sd($\mathbf{r}$) in salinity around 100 m and in temperature at all depths, whereas B1R2 displays slightly smaller sd($\mathbf{d}$) in both temperature and salinity in the upper 100 m. This illustrates that a better fit to the data (achieved in B1R1 by reducing σ^o) does not necessarily translate into a better model forecast. The differences arising from using the ensemble σ^b (B2R2; dashed curves) are larger, with both sd($\mathbf{r}$) and sd($\mathbf{d}$) being increased relative to those in B1R1 and B1R2, especially near the surface.

At first sight it appears that the use of the ensemble σ^b has slightly degraded the performance of the assimilation system. Closer inspection of Fig. 7, however, reveals that, while the innovations are larger in B2R2, the difference between the residuals and innovations is smaller than in B1R1 and B1R2, particularly in the upper 100 m where the difference is 0.1°C and 0.05 psu smaller. This result then suggests that the rate of loss of information between 10-day assimilation cycles is smaller in B2R2 than in B1R1 and B1R2. This can be quantified by considering the relative percentage difference between the standard deviation of the innovation vector and that of the actual residual ($\tilde{\mathbf{r}}$): $R = 100 \times \{\mathrm{sd}(\mathbf{d}) - \mathrm{sd}(\tilde{\mathbf{r}})\}/\mathrm{sd}(\mathbf{d})$. This diagnostic can be appreciated only in combination with Fig. 7 which measures the actual fit to the data. For example, the control has zero information loss ($R = 0$ since $\mathrm{sd}(\tilde{\mathbf{r}}) = \mathrm{sd}(\mathbf{d})$) but is clearly inferior to the assimilation experiments in terms of the fit to the data. Figure 8 shows vertical profiles of R for temperature (left panel) and salinity (right panel). The information loss rate in B2R2 is smallest at all depths, with values ranging between 5%–6% for temperature and 9%–17% for salinity. The error growth rates are considerably larger in B1R1 and B1R2, especially above 150 m, where values reach up to 18% (respectively, 14%) for temperature and 45% (respectively, 33%) for salinity.

(a) Temperature   (b) Salinity
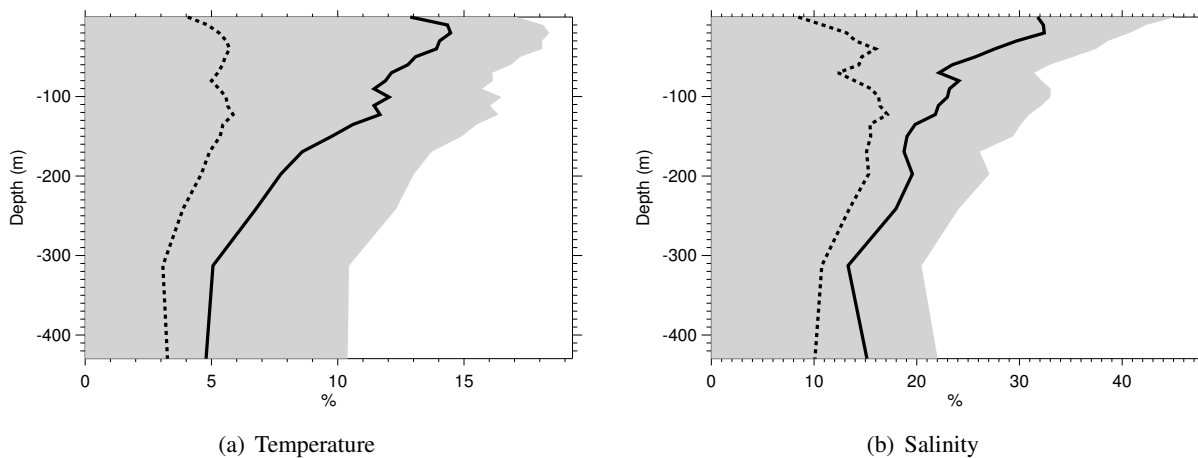
Figure 8: Vertical profiles of the information loss rate $R = 100 \times \{\mathrm{sd}(\mathbf{d}) - \mathrm{sd}(\tilde{\mathbf{r}})\}/\mathrm{sd}(\mathbf{d})$ for temperature (left panel) and salinity (right panel) in B1R1 (grey shaded areas), B1R2 (solid curves) and B2R2 (dashed curves).

5.4 Specified versus diagnosed σ^b and σ^o

The difficulty in defining background- and observation-error statistics means that they are likely to be incorrectly specified in a practical data assimilation system. Desroziers *et al.* (2005) discuss how the innovations and analysis increments generated by a data assimilation system can be used to diagnose *a posteriori* the covariances of observation error and background error in observation space. Assuming that the background and observation errors are mutually uncorrelated, and that their covariance matrices are good approximations to the

true error covariance matrices, then the covariance matrix of the innovation vector satisfies

$$E[\mathbf{d}\mathbf{d}^T] \;\approx\; \mathbf{HB}_{(\mathbf{w})}\mathbf{H}^T + \mathbf{R}. \tag{20}$$

This classical result is easily derived using the expression for the innovation vector in terms of the background and observation errors, given by (45) in Appendix B. Furthermore, using the analysis equation (43), it is straightforward to show that the individual components of (20) satisfy

$$E[\mathbf{d}\,(\mathbf{H}\delta\mathbf{w}^a)^T] \;\approx\; \mathbf{HB}_{(\mathbf{w})}\mathbf{H}^T \tag{21}$$

and

$$E[\mathbf{d}\,(\mathbf{d}-\mathbf{H}\delta\mathbf{w}^a)^T] \;\approx\; \mathbf{R}. \tag{22}$$

The left-hand sides of (21) and (22) can be estimated using statistics from the assimilation system, while the right-hand sides of these equations are the specified covariance matrices discussed earlier. In this section, these expressions are used to check the consistency of the specified *standard deviations* (σ^b and σ^o) with those diagnosed using assimilation statistics. The analysis focuses on the time- and horizontally-averaged component of the standard deviations. As in (19), the mean bias has been removed from $\mathbf{d}$ and $\mathbf{H}\delta\mathbf{w}^a$ in estimating the standard deviations from (21) and (22).

Figure 9 shows vertical profiles from B2R2 of the specified σ^b and σ^o (solid curves) and the diagnosed σ^b and σ^o (dashed curves) estimated from (21) and (22) using the innovation and analysis increments from all cycles between 1994-2000. The specified σ^b are identical to those displayed earlier in Fig. 5 (dashed curves). In B2R2, the specified σ_T^b and σ_S^b are everywhere *underestimated* compared to the diagnosed values (Figs. 9a and c), whereas the specified σ_T^o and σ_S^o are *overestimated* compared to the diagnosed values, apart from the upper 30 m where the σ_S^o are slightly underestimated (Figs. 9b and d). The maximum specified-minus-diagnosed differences are -0.45°C and -0.4 psu for σ_T^b and σ_S^b, and 0.4°C and 0.15 psu for σ_T^o and σ_S^o. It is interesting to note that the structure and amplitude of the diagnosed σ_T^b, and to a lesser extent the diagnosed σ_S^b, are closer to those of the parameterized σ_T^b and σ_S^b than the ensemble σ_T^b and σ_S^b (cf. Fig. 5). The ensemble and diagnosed σ_S^b in particular exhibit large differences in the upper 200 m. Compared to B2R2, there is better consistency between the diagnosed and specified σ^b in B1R2 (Figs. 10a and c), although this seems to be achieved at the expense of degrading the consistency between the diagnosed and specified σ^o (Figs. 10b and d).

The results in Fig. 9 suggest that the ensemble 3D-Var system produces background (and analysis) perturbations with inadequate spread on a global average. This apparent deficiency is not unique to our system but is a common problem in other ensemble data assimilation systems as well (e.g., see Houtekamer and Mitchell (2005) for a discussion within the context of the EnKF). This issue is discussed further in section 6. The apparent overestimation of σ^o, on the other hand, points to limitations in our simple model of the observation error statistics, which ignores spatial and temporal correlations and employs time-independent variance estimates derived from a method that is itself subject to assumptions of questionable validity. Care must be taken, however, in interpreting Fig. 9 since the diagnosed σ^b and σ^o are not necessarily the optimal values of σ^b and σ^o that should have been specified. Any attempt to adjust σ^b or σ^o on the basis of (21) and (22) will ultimately lead to a new set of innovations and analysis increments which in turn will lead to new diagnostic estimates of σ^b and σ^o. The procedure for adjusting σ^b and/or σ^o is thus iterative and inherently nonlinear, with no guarantee of convergence. Desroziers *et al.* (2005) present an adaptive algorithm that employs (21) and (22) to update the background-error variances (at observation points) and observation-error variances in a cycled assimilation system. We have made no attempt to apply the method in the current study but it offers an interesting possibility for improving the variance estimates in future applications of our assimilation system. Furthermore, as pointed out by Talagrand (1999), consistency between the diagnosed and specified statistics is neither a necessary nor a sufficient condition for optimality of the assimilation system. Indeed, as shown later in section 5.6, comparing the analyses with observations that were not assimilated indicates that B2R2 is superior to B1R2 despite having poorer internal consistency in the σ^b statistics.

(a) Specified and diagnosed σ_T^b

(b) Specified and diagnosed σ_T^o

(c) Specified and diagnosed σ_S^b

(d) Specified and diagnosed σ_S^o
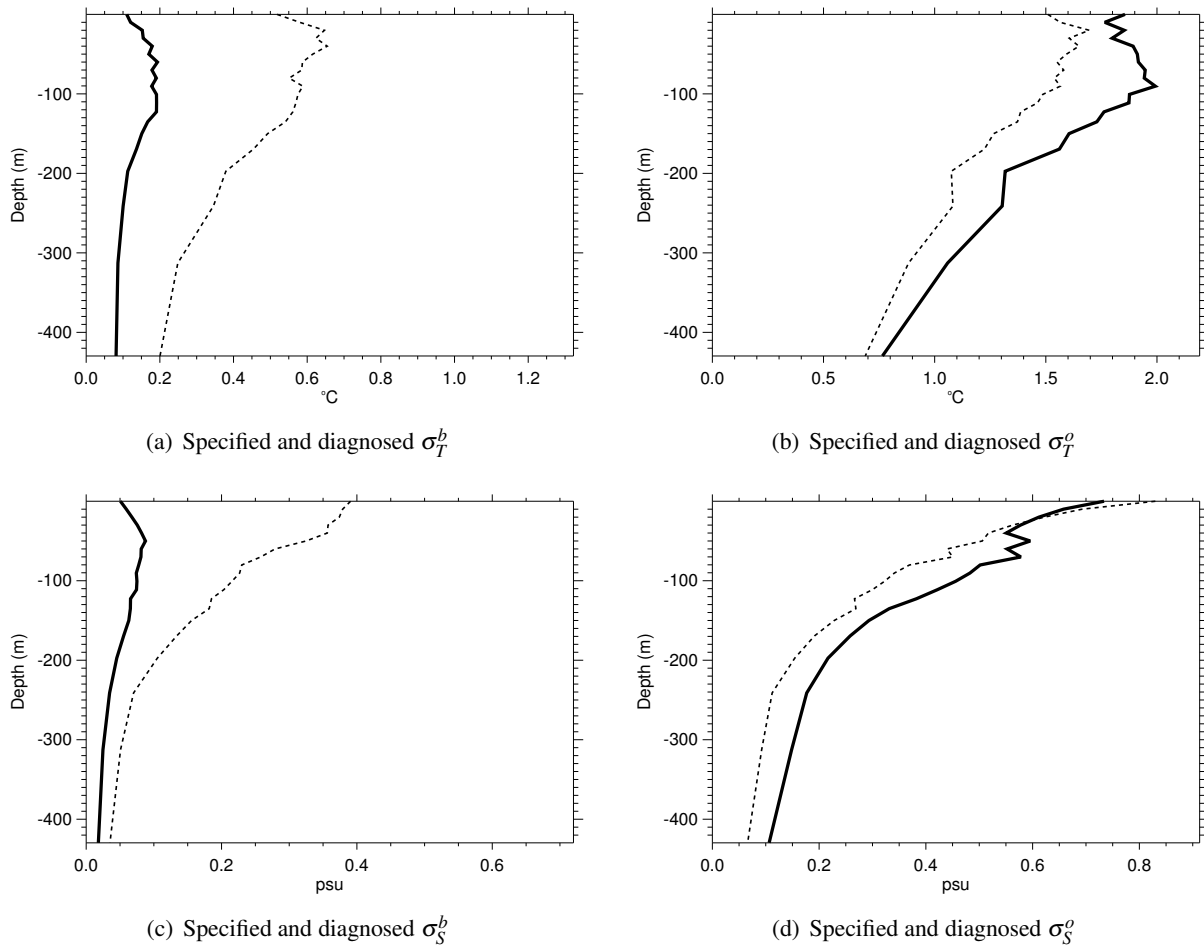
Figure 9: Vertical profiles of σ^b (left panels) and σ^o (right panels) for temperature (upper panels) and salinity (lower panels) in B2R2. Solid curves correspond to the σ^b and σ^o that were specified in the assimilation experiment; dashed curves correspond to the σ^b and σ^o that were diagnosed a posteriori using (21) and (22). The specified σ^b and σ^o are identical to those displayed by dashed curves in Fig. 5.

(a) Specified and diagnosed σ_T^b

(b) Specified and diagnosed σ_T^o

(c) Specified and diagnosed σ_S^b

(d) Specified and diagnosed σ_S^o
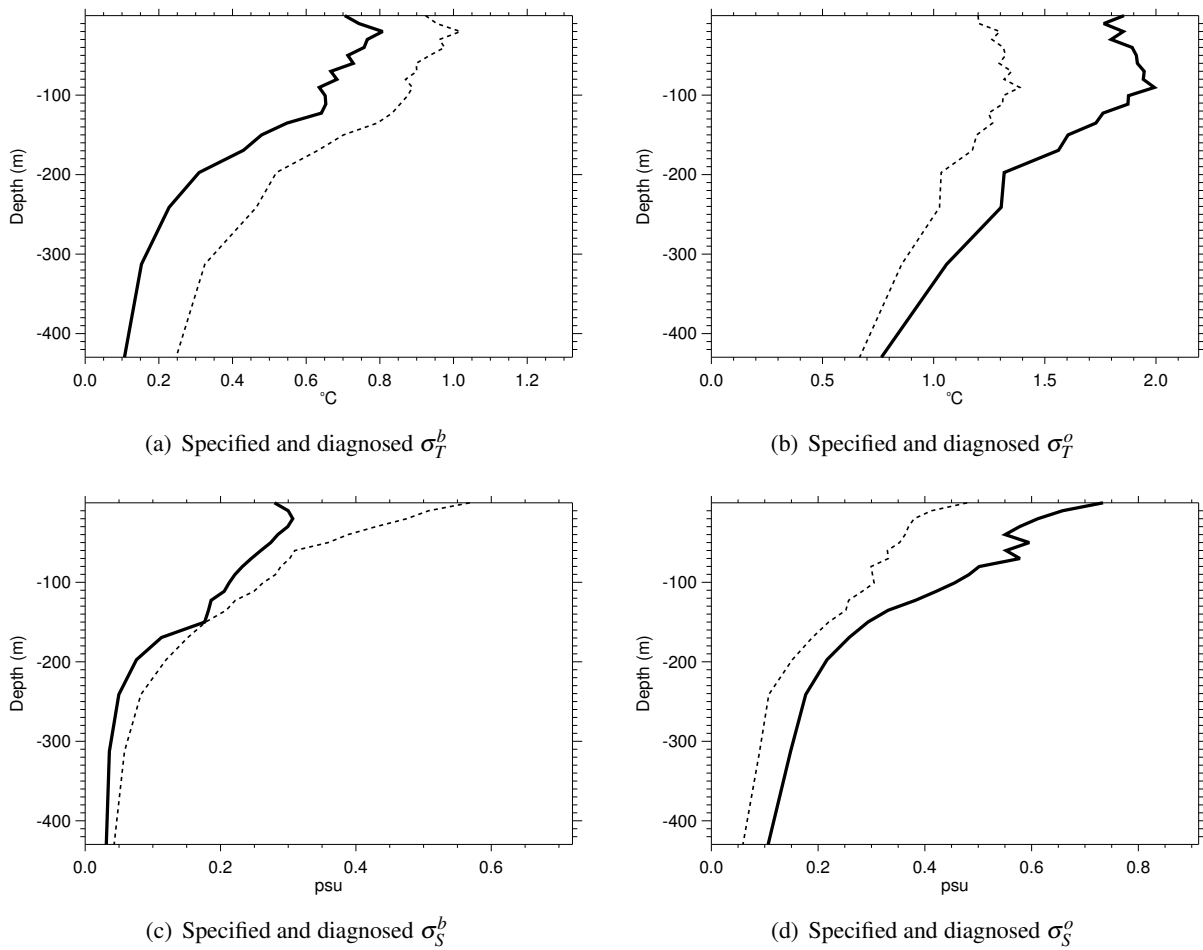
Figure 10: Same as Fig. 9 but for B1R2.

5.5 Temporal variability of the ensemble and assimilation statistics

The results presented so far have highlighted time-averaged aspects of the assimilation performance. In this section, time-varying aspects will now be evaluated, focusing on results from the ensemble experiment B2R2. Figures 11a and b show time-series of the 1993-2000 ensemble *spread* (the square root of the ensemble variance) of the observation-space analysis $\mathbf{H}_i\mathbf{w}_l^a(t_i)$ (light grey shade) and background $\mathbf{H}_i\mathbf{w}_l^b(t_i)$ (black shade), computed with respect to all ensemble members $l = 0, \ldots, 8$:

$$\text{spread}\{\mathbf{H}_i\mathbf{w}^{a,b}\} = \sqrt{\overline{\frac{1}{8}\sum_{l=0}^{8}\left(\mathbf{H}_i\mathbf{w}_l^{a,b}(t_i) - \frac{1}{8}\sum_{l=0}^{8}\mathbf{H}_i\mathbf{w}_l^{a,b}(t_i)\right)^2}} \qquad (23)$$

where the overbar indicates spatial average over the globe and within vertical model grid cells, and temporal average over 30-day intervals. A well-defined ensemble should have a spread characteristic of the actual uncertainty in the model state. Figures 11a and b show that the spread in both temperature and salinity is systematically smaller in the analysis than in the background, as one would expect. The spread appears to stabilize around mean values of $0.1°C$ and 0.035 psu, after an initial increase during the first 6 months of the experiment. In other words, there is no evidence of ensemble collapse. The decrease in the spread from mid-1993 onwards corresponds to the time when the parameterized σ^b are replaced with the ensemble σ^b. The variability of the spread is larger for salinity than for temperature, which is mainly associated with increased sampling error due to the fewer number of salinity observations. It is interesting to note that the values of the mean spread are similar to those computed in the stochastic EnKF system of Leeuwenburgh (2007) (see his Fig. 3 for the tropical Pacific region). His system was based on a different ocean model as well as a different assimilation method, but employed a similar perturbation strategy to ours, involving random perturbations to the atmospheric forcing fields and observations.

Figures 11c and d show corresponding time-series of the $\text{sd}(\tilde{\mathbf{r}}_i)$ (light grey shade) and innovation $\text{sd}(\mathbf{d}_i)$ (black shade) of the unperturbed ensemble member $l = 0$, as given by (19) but with the temporal averaging operator defined as in (23). Both $\text{sd}(\tilde{\mathbf{r}}_i)$ and $\text{sd}(\mathbf{d}_i)$ are about one order of magnitude larger than the spread of the (observation space) analysis and background (upper panels). The spread of the background state at observation points roughly corresponds to the prescribed values of σ^b at observation points, as can be seen by comparing the magnitudes of the temperature and salinity spread in Figs. 11a and b with those of the prescribed mean σ_T^b and σ_S^b profiles in Figs. 5a and c (dashed curves). For both temperature and salinity, the magnitude of $\text{sd}(\mathbf{d}_i)$ is at all times comparable to that of the mean σ^o in Figs. 5b and d, which is consistent with (20) in view of the relatively small ensemble spread that defines σ^b. Despite the small spread, $\text{sd}(\mathbf{d}_i)$ (and $\text{sd}(\tilde{\mathbf{r}}_i)$) of B2R2 is consistently much smaller than $\text{sd}(\mathbf{d}_i)$ of CTL (dark grey shade). The variability in CTL and B2R2 is relatively coherent, especially for temperature which displays an annual cycle with smallest $\text{sd}(\mathbf{d}_i)$ (and $\text{sd}(\tilde{\mathbf{r}}_i)$) in the boreal winter.

5.6 Comparison with independent data

The diagnostics presented in the previous sections have focused on the model variables (temperature and salinity) that are directly constrained by the observations. In this section, model variables (SSH and velocity) that are not directly constrained by the observations are examined and validated against independent data. Table 2 shows correlation coefficients and Root-Mean-Square (RMS) errors of the 1993-2000 SSH anomalies between TOPEX/POSEIDON (T/P) and those of the various experiments. The regions considered are the northwest extratropical Atlantic ($75°W$-$40°W$, $30°N$-$60°N$) and NINO3.4 ($170°W$-$120°W$, $5°S$-$5°N$) in the tropical Pacific. In the northwest extratropical Atlantic, the CTL has the highest correlation and lowest RMS error of all experiments, which suggests that data assimilation is degrading the SSH field to some extent in this region. Of

(a) Temperature spread

(b) Salinity spread

(c) Temperature residual and innovation vector

(d) Salinity residual and innovation vector
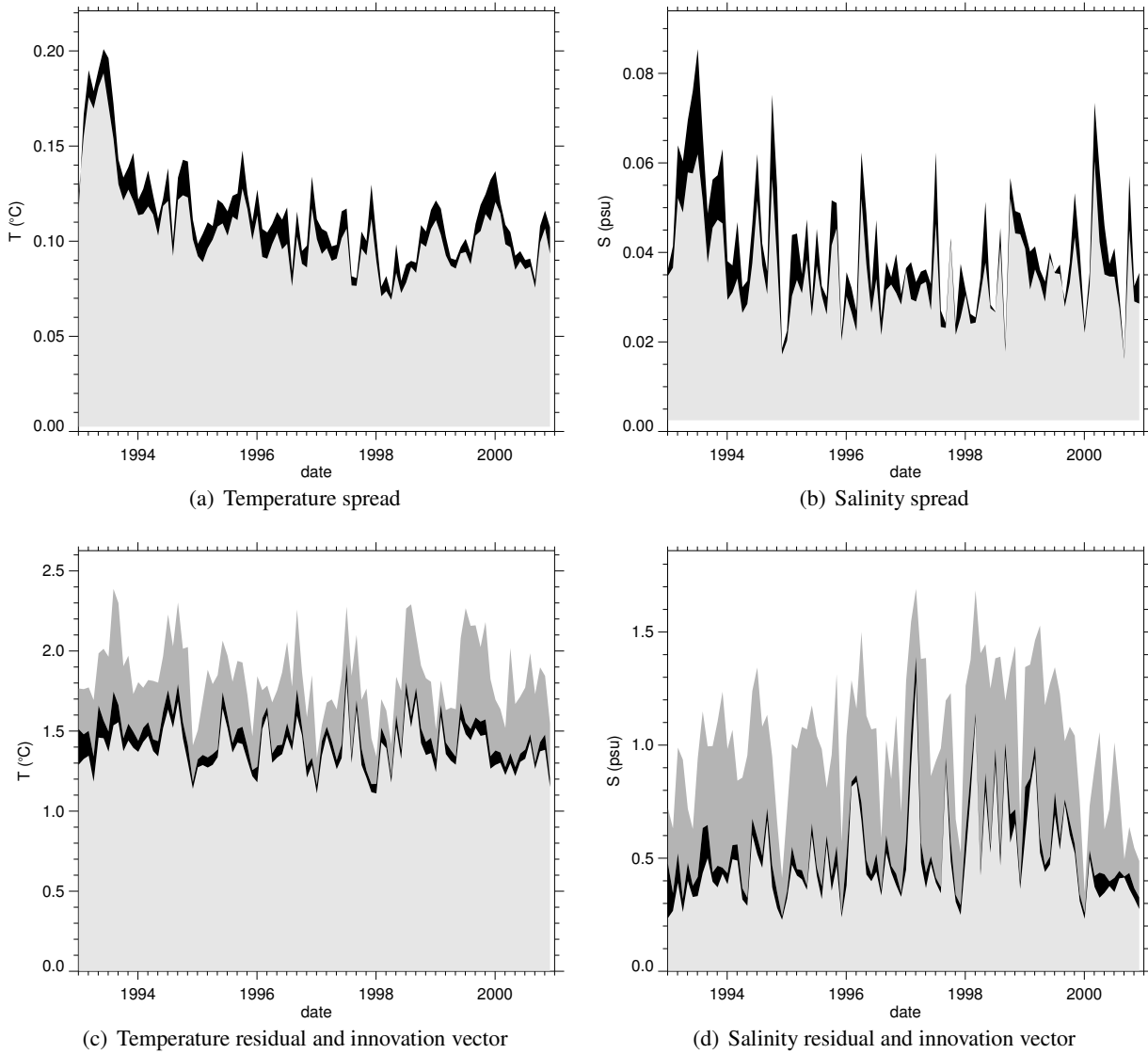
Figure 11: Upper panels: 1993-2000 time-series of the ensemble spread at observation points (upper panels) for the background, $\mathbf{H}_i\mathbf{w}^b(t_i)$ (black shaded area), and analysis, $\mathbf{H}_i\mathbf{w}^a(t_i)$ (light grey shaded area), in B2R2. Lower panels: 1993-2000 time-series of the standard deviation of the innovation vector, $sd(\mathbf{d}_i)$ (black shaded area), and of the residuals, $sd(\tilde{\mathbf{r}}_i)$ (light grey shaded area), in B2R2. The standard deviation of the innovation in CTL (dark grey shaded area) is also shown. Temperature and salinity are displayed in the left and right panels, respectively. Values have been been computed for the global region and averaged into 30-day intervals.

the assimilation experiments, B2R2 compares best with T/P, while B1R1 compares worst. Since the closest fit to the *in situ* data was achieved in B1R1, followed by B1R2 and then B2R2 (see Figs. 6 and 7), this further suggests that the SSH field degrades in this region as the model fit to the *in situ* data improves. In contrast, in NINO3.4, the assimilation experiments give similar statistical performance. Relative to CTL, they exhibit a slight improvement in correlation (the correlation of CTL is already very high) and a larger reduction in the RMS error.

The 1993-2000 time-series of the SSH anomalies in these regions, displayed in Fig. 12, show clearly that the dominant variability is seasonal in the northwest extratropical Atlantic (Fig. 12a) and interannual in the tropical Pacific (Fig. 12b). Compared to T/P (thin solid curve), the seasonal variations in the northwest extratropical Atlantic are reproduced in the assimilation experiments but with smaller amplitude, especially in B1R2 (thick solid curve) during 1996-1998. The observed seasonal variability is better reproduced in B2R2 (dashed curve). Experiment B1R2 also displays a pronounced decreasing trend after 1999, which is weaker in B2R2 and not present in T/P. In NINO3.4, the interannual variations of CTL are slightly damped relative to those in T/P, especially during the 1997 El Niño event where the assimilation experiments, especially B1R2, reproduce the large amplitude of the observed SSH anomalies much better.

	NW.EXTROP.ATL		NINO3.4	
Experiment name	Correlation	RMS error (m)	Correlation	RMS error (m)
CTL	0.97	0.012	0.98	0.022
B1R1	0.62	0.040	0.99	0.012
B1R2	0.73	0.033	0.99	0.012
B2R2	0.87	0.023	0.99	0.013

Table 2: Correlation coefficient and RMS error (in metres) in the northwest extratropical Atlantic (75°W-40°W, 30°N-60°N) and NINO3.4 region of the tropical Pacific (170°W-120°W, 5°S-5°N) between SSH anomalies from T/P data and those from the model in the various experiments.

At the equator in the Pacific, the quality of the velocity field can be assessed by comparing it to current meter data from the TAO array. Figure 13 shows vertical profiles of the correlation coefficients and RMS errors between zonal current data from TAO at three locations (165°E, 140°W and 110°W) and the corresponding zonal velocity field from CTL (dotted curves), B1R2 (solid curves) and B2R2 (dashed curves). The assimilation of temperature and salinity profiles improves the intensity of the equatorial surface currents and equatorial undercurrent in the central Pacific, as indicated by the reduced RMS errors in B1R2 and B2R2 compared to those of CTL in the upper 100 m at 140°W (Fig. 13e). The upper ocean currents in B2R2 are also improved relative to CTL in the eastern Pacific (Figs. 13c and f) but slightly degraded in the western Pacific (Figs. 13a and d). The zonal currents in B1R2 are degraded in the upper 150 m of the western Pacific (Figs. 13a and d), and show no clear improvement over CTL in the eastern Pacific (Figs. 13c and f). Experiment B2R2 outperforms B1R2 at nearly all depths at all three locations.

6　Summary and conclusions

A 3D-Var system for global ocean analysis has been described in this paper. The global 3D-Var system is based on an earlier 3D-Var system for the tropical Pacific (Weaver *et al.* 2003; Vialard *et al.* 2003) but includes many new features such as a fully multivariate background-error covariance model (Weaver *et al.* 2005), the use of a state-of-the-art quality-controlled *in situ* data-set (Ingleby and Huddleston 2007), revised background- and observation-error variance formulations, and the capacity to generate ensembles of ocean analyses. On a
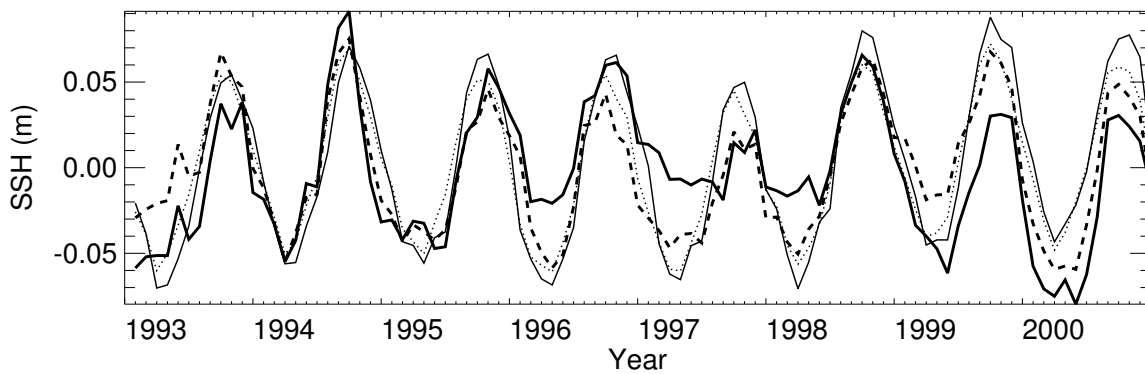
(a) SSH anomaly in NW.EXTROP.ATL
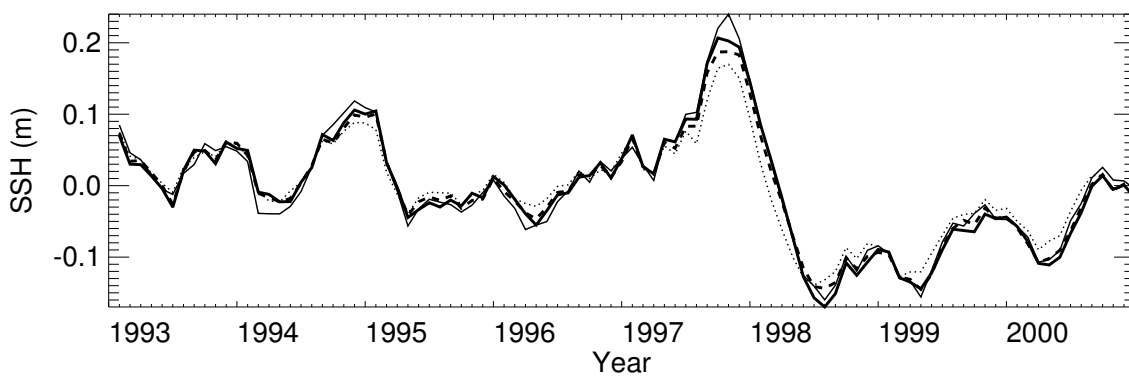
(b) SSH anomaly in NINO3.4

Figure 12: 1993-2000 time-series of SSH anomalies in the northwest extratropical Atlantic (upper panel) and NINO3.4 region of the tropical Pacific (lower panel) from CTL (dotted curve), B1R2 (thick solid curve), B2R2 (dashed curve), and T/P (thin solid curve).
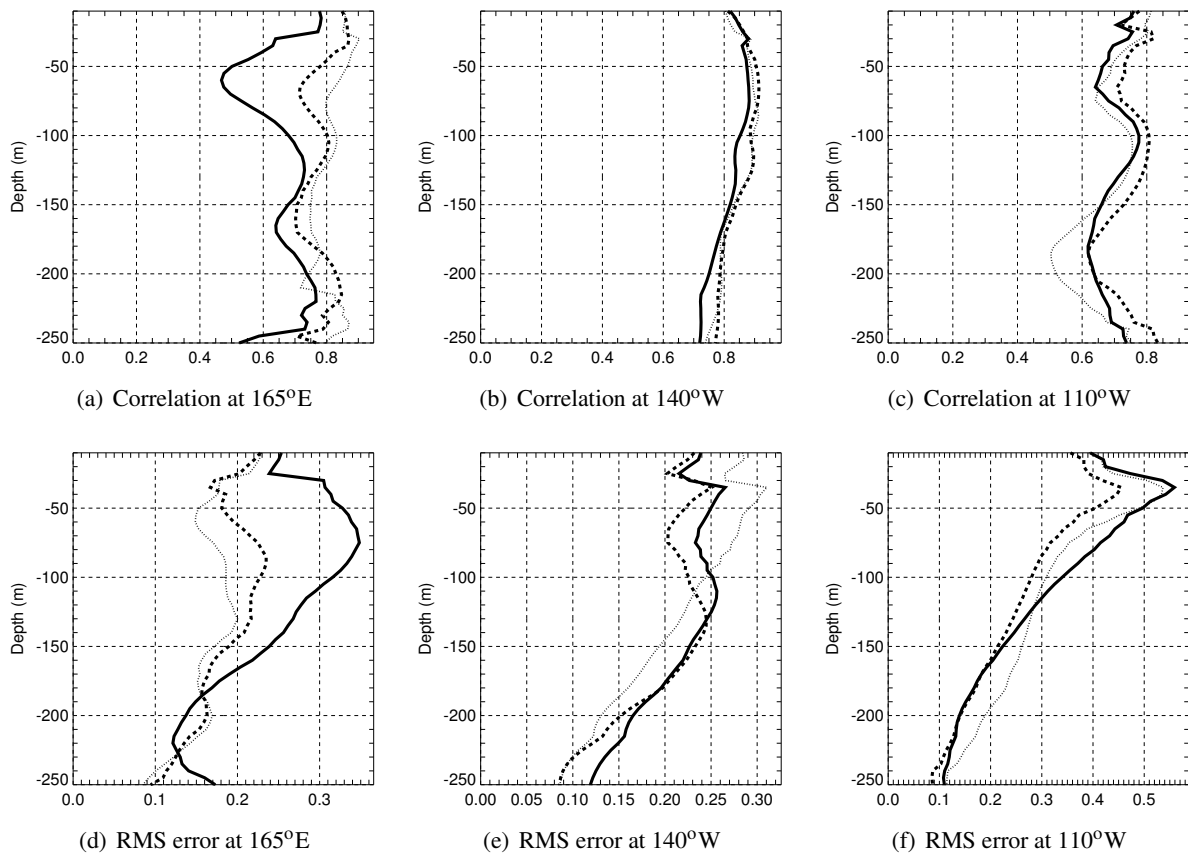
Figure 13: Correlation (upper panels) and RMS error (m s^{-1}; *lower panels) between equatorial zonal currents from TAO data and those from CTL (dotted curves), B1R2 (solid curves) and B2R2 (dashed curves) over the 1993-2000 period at 165ºE (left panels), 140ºW (middle panels) and 110ºW (right panels).*

given assimilation cycle, the ensemble of analyses are created by adding perturbations to the surface forcing fields (wind-stress, fresh-water flux, and SST - a proxy for heat flux) and observations (temperature and salinity profiles) used in the assimilation process. These perturbations are based on estimates of the actual uncertainty in these input fields. The ocean initial conditions on each cycle are also perturbed, but this is done implicitly as a result of the parallel cycling of the 3D-Var system with different perturbed forcing and observations for each ensemble member. The purpose of the analysis ensemble is to sample uncertainty in the ocean model state. Applications of the analysis ensemble include initialization of coupled ocean-atmosphere models for probabilistic climate forecasting, uncertainty estimation for historical ocean reanalysis, and the estimation of flow-dependent background-error covariances.

The main purpose of this paper was to explore the use of the ensemble 3D-Var for providing flow-dependent estimates of the background-error *standard deviations* (σ^b). A 9-member ensemble was constructed and tested in a cycled 3D-Var framework over the period 1993-2000. On each 10-day cycle, the σ^b of all members were updated based on the ensemble spread of background states. To reduce sampling error, a 9-cycle (90-day) sliding window was used to include additional ensemble members from the recent past in the σ^b computation. The larger sample size (81 in total) was achieved at the expense of filtering out intraseasonal variations in background error. This constraint could be relaxed in the future by increasing the number of ensemble members and/or by employing alternative filtering techniques for reduced sampling noise, such as those described in recent articles by Buehner and Charron (2007) and Berre *et al.* (2007).

A control experiment, in which no data were assimilated, produced large differences in the mean state and variability of the temperature and salinity fields when compared to the profile observations that were assimilated in the 3D-Var experiment. These differences were substantially reduced in the ensemble 3D-Var experiment. Evaluation of fields not directly constrained by the assimilated observations gave mixed results. Results showed that, in general, the ensemble 3D-Var experiment improved equatorial currents in the central and eastern Pacific and the representation of interannual variability of SSH. However, there were other regions where the assimilation degraded the results (equatorial currents in the western Pacific, SSH anomalies in the northwest Atlantic), possibly because of problems related to large systematic model error in these regions. Comparisons with a separate 3D-Var experiment that employed a simpler, empirically-based flow-dependent σ^b parameterization showed that, on the global average, both led to similar reductions in the profile innovations (the mean and standard deviation) below 150 m but the parameterized σ^b gave slightly smaller innovations above 150 m. Fields not directly constrained by the assimilated observations, however, were clearly better (closer to independent observations) with the ensemble σ^b than with the parameterized σ^b. Moreover, the rate of loss of information between assimilation cycles, as measured by the relative difference between the innovation vector and the analysis residual, was much reduced using the ensemble σ^b suggesting that the ensemble σ^b produced analyses that were in better balance than those generated using the parameterized σ^b. This result could have important implications on the degree to which the assimilated information is retained by the model during the forecast step, but further investigation of this issue is needed; e.g., by computing statistics of the observation-minus-background differences on time periods that go beyond the 10-day forecast cycling period, or by testing the impact on seasonal forecasts using coupled models.

Diagnostics designed to check the consistency of the prescribed covariances with those estimated *a posteriori* from assimilation statistics indicated that the σ^b above 150 m were underestimated by the ensemble. Simple procedures to inflate the ensemble-generated σ^b in the upper ocean were tested (results not presented in this study) but did not give satisfactory results. The apparent underestimation of the ensemble spread is likely due to several factors including the small size of the ensemble and deficiences in the perturbation strategy. The SST relaxation term, for example, has the tendency to produce excessive damping of temperature perturbations near the surface. The direct assimilation of SST data (via the cost function), which will be implemented in future versions of our assimilation system, should alleviate this problem. The absence of model-error perturbations is

also a weakness, particularly for the relatively low-resolution model used in this study which can be expected to have a significant model-error component associated with the unresolved mesoscale. Techniques to include model-error perturbations, such as those described by Hamill and Whitaker (2005), could be explored in future work. Despite these apparent shortcomings, results from this study are encouraging and suggest that useful information about background error can be extracted from a suboptimal ensemble.

This study has focused on using the ensemble to estimate the background-error standard deviations, but other parameters of the background-error covariance model could be estimated as well. Pannekoucke *et al.* (2008) present a practical method for estimating geographically dependent correlation length scales from ensemble differences. In our quasi-Gaussian correlation model based on a generalized diffusion operator, these length scales are related to the elements of the diffusion tensor (Pannekoucke and Massart 2008). Preliminary results from applying the Pannekoucke *et al.* method to estimate the tensor elements from time-averaged ensembles generated by our system are encouraging although further work is needed to evaluate the impact of the new length scale estimates in a cycled assimilation experiment.

The ensemble procedure has been tested in a 3D-Var framework in this study but is applicable to 4D-Var as well. Practical 4D-Var applications, however, would likely require approximations in the ensemble-generation strategy due to the substantial extra cost of 4D-Var. In general, the extra computational expense of producing ensembles of analyses may be justified if these analyses can be used simultaneously for probabilistic forecasting as well as background-error covariance estimation.

7   Acknowledgements

A   Observation-error covariance estimation using the Fu *et al.* method

Following Janjíc and Cohn (2006), we define the true state vector $\mathbf{x}^t(t_i)$ at time t_i to be the component $\Pi_{(\mathbf{x})}\mathbf{x}^t_C(t_i)$ of the true continuum state $\mathbf{x}^t_C(t_i)$ where $\Pi_{(\mathbf{x})}$ is a projection operator from the continuum onto the finite-dimensional subspace resolved by the numerical model. The resolved component is the quantity that we wish to estimate through data assimilation. The observation vector $\mathbf{y}^o_i$ can be related to $\mathbf{x}^t(t_i)$ through an equation of the form (Janjíc and Cohn 2006)

$$\mathbf{y}^o_i = \mathbf{H}_i\mathbf{x}^t(t_i) + \varepsilon^m_i + \varepsilon^r_i + \varepsilon^i_i \tag{24}$$

where $\mathbf{H}_i$ is the discrete observation operator which is taken to be linear as in the assimilation system described in section 3. The discrepancy between $\mathbf{y}^o_i$ and $\mathbf{H}_i\mathbf{x}^t(t_i)$ can be attributed to errors in the measurement process, ε^m_i, representativeness errors associated with the unresolved scales, $\varepsilon^r_i = \mathscr{H}_i[\mathbf{x}^t_C(t_i) - \mathbf{x}^t(t_i)]$, where $\mathscr{H}_i$ is the continuum observation operator, and interpolation errors associated with approximating the continuum observation operator by $\mathbf{H}_i$, $\varepsilon^i_i = (\mathscr{H}_i - \mathbf{H}_i)\mathbf{x}^t(t_i)$. The sum of these errors is the total observation error,

$$\varepsilon^o_i = \varepsilon^m_i + \varepsilon^r_i + \varepsilon^i_i. \tag{25}$$

The method of Fu *et al.* (1993) is designed to estimate the static component of the observation-error covariance matrix by comparing time-averaged statistics of the observation vector with those of its model equivalent $\mathbf{H}_i \mathbf{x}^c(t_i)$ where $\mathbf{x}^c(t_i)$ is the state vector computed from a model integration without data assimilation (the control run in this study). At any time t_i, the unconstrained model state can be related to the true state through

$$\mathbf{x}^c(t_i) = \mathbf{x}^t(t_i) + \varepsilon^c(t_i) \tag{26}$$

where $\varepsilon^c(t_i)$ represents the unconstrained model-state error. For notational convenience, the time parameter will be dropped in the rest of this appendix. Using (24)-(26), the auto- and cross-covariances of $\mathbf{y}^o$ and $\mathbf{H}\mathbf{x}^c$ can be computed as follows:

$$E\left[\tilde{\mathbf{y}}^o (\tilde{\mathbf{y}}^o)^T\right] = \mathbf{H}E\left[\tilde{\mathbf{x}}^t(\tilde{\mathbf{x}}^t)^T\right]\mathbf{H}^T + E\left[\varepsilon^o(\varepsilon^o)^T\right] + \mathbf{H}E\left[\tilde{\mathbf{x}}^t(\varepsilon^o)^T\right] + E\left[\varepsilon^o(\tilde{\mathbf{x}}^t)^T\right]\mathbf{H}^T, \tag{27}$$

$$E\left[\mathbf{H}\tilde{\mathbf{x}}^c (\mathbf{H}\tilde{\mathbf{x}}^c)^T\right] = \mathbf{H}E\left[\tilde{\mathbf{x}}^t(\tilde{\mathbf{x}}^t)^T\right]\mathbf{H}^T + \mathbf{H}E\left[\varepsilon^c(\varepsilon^c)^T\right]\mathbf{H}^T + \mathbf{H}E\left[\tilde{\mathbf{x}}^t(\varepsilon^c)^T\right]\mathbf{H}^T + \mathbf{H}E\left[\varepsilon^c(\tilde{\mathbf{x}}^t)^T\right]\mathbf{H}^T, \tag{28}$$

$$E\left[\tilde{\mathbf{y}}^o (\mathbf{H}\tilde{\mathbf{x}}^c)^T\right] = \mathbf{H}E\left[\tilde{\mathbf{x}}^t(\tilde{\mathbf{x}}^t)^T\right]\mathbf{H}^T + \mathbf{H}E\left[\tilde{\mathbf{x}}^t(\varepsilon^c)^T\right]\mathbf{H}^T + E\left[\varepsilon^o(\varepsilon^c)^T\right]\mathbf{H}^T + E\left[\varepsilon^o(\tilde{\mathbf{x}}^t)^T\right]\mathbf{H}^T \tag{29}$$

where $E[\ ]$ denotes the expectation operator and $\tilde{\mathbf{z}} = \mathbf{z} - E[\mathbf{z}]$. The errors are assumed to be unbiased: $E[\varepsilon^o] = E[\varepsilon^c] = 0$. The *unknown* auto-covariance of the true state, $E[\tilde{\mathbf{x}}^t(\tilde{\mathbf{x}}^t)^T]$, can be eliminated by subtracting (29) from (27) and (28) to yield

$$E\left[\tilde{\mathbf{y}}^o (\tilde{\mathbf{y}}^o - \mathbf{H}\tilde{\mathbf{x}}^c)^T\right] = E\left[\varepsilon^o(\varepsilon^o)^T\right] + \mathbf{Z}_1, \tag{30}$$

$$E\left[\mathbf{H}\tilde{\mathbf{x}}^c (\tilde{\mathbf{y}}^o - \mathbf{H}\tilde{\mathbf{x}}^c)^T\right] = -\mathbf{H}E\left[\varepsilon^c(\varepsilon^c)^T\right]\mathbf{H}^T + \mathbf{Z}_2, \tag{31}$$

where

$$\mathbf{Z}_1 = \mathbf{H}E\left[\tilde{\mathbf{x}}^t(\varepsilon^o)^T\right] - E\left[\varepsilon^o(\varepsilon^c)^T\right]\mathbf{H}^T - \mathbf{H}E\left[\tilde{\mathbf{x}}^t(\varepsilon^c)^T\right]\mathbf{H}^T, \tag{32}$$

$$\mathbf{Z}_2 = E\left[\varepsilon^o(\tilde{\mathbf{x}}^t)^T\right]\mathbf{H}^T + E\left[\varepsilon^o(\varepsilon^c)^T\right]\mathbf{H}^T - \mathbf{H}E\left[\varepsilon^c(\tilde{\mathbf{x}}^t)^T\right]\mathbf{H}^T. \tag{33}$$

The left-hand sides of (30) and (31) are quantities that can be estimated, under the ergodic assumption, from time- and spatially-averaged observations and their unconstrained model counterpart. The unknown quantity of interest here is the observation-error covariance matrix, $\widehat{\mathbf{R}} \equiv E[\varepsilon^o(\varepsilon^o)^T]$, in (30).

Following Fu *et al.* (1993), an approximate equation for $\widehat{\mathbf{R}}$ is obtained by assuming that $\mathbf{Z}_1 \approx 0$ or at least that this term is small (in a matrix-norm sense) compared to $\widehat{\mathbf{R}}$. The validity of this assumption can be appreciated by examining each term in (32). The first term can be neglected by assuming that the true state (the resolved scales) and observation error are approximately uncorrelated, $E[\tilde{\mathbf{x}}^t(\varepsilon^o)^T] \approx 0$. This is a safe assumption for the measurement component of the observation error which has no reason to be correlated with the true state. It also implies that the resolved and unresolved scales are entirely decoupled, which is more restrictive. The second term can be neglected by assuming that the observation error and unconstrained model-state error are approximately uncorrelated, $E[\varepsilon^o(\varepsilon^c)^T] \approx 0$. From (26), this is ensured if $E[\varepsilon^o(\tilde{\mathbf{x}}^t)^T] \approx 0$, as already discussed above, and if $E[\varepsilon^o(\tilde{\mathbf{x}}^c)^T] \approx 0$, which is a reasonable assumption since the model (control) integration is not constrained by the observations. It is more difficult, however, to justify ignoring the third term ($E[\tilde{\mathbf{x}}^t(\varepsilon^c)^T] \approx 0$), as already pointed out by Menemenlis and Chechelnitsky (2000) who provide evidence in their analysis of TOPEX/POSEIDON altimeter data that suggests that this term is not negligible. This third assumption is made purely for practical convenience and should be treated with caution. Equation (30) (with $\mathbf{Z}_1 = 0$) has been used in this study to estimate the variances of observation error (see (11)) although in principle it could be used to estimate the correlations as well.

The assumptions described above also imply that $\mathbf{Z}_2 \approx 0$ in (31), thereby yielding an approximate expression for $\mathbf{H}\mathbf{B}_{(\mathbf{x}^c)}\mathbf{H}^T$ where $\mathbf{B}_{(\mathbf{x}^c)} \equiv E[\varepsilon^c(\varepsilon^c)^T]$. Equation (31) may provide useful information for initializing the background-error covariance matrix on the first assimilation cycle, where the background state is obtained from

an unconstrained model (spin-up) integration, but is of questionable relevance for defining background-error covariances in the presence of data assimilation. This expression has not been exploited in this study where instead the ensemble method has been used to enrich a quasi-static covariance model with flow-dependent estimates of the variances.

B   Background-error covariance estimation using an ensemble method

The purpose of this appendix is to illustrate how differences between members of a suitably generated 3D-Var ensemble can be used to estimate the covariances of background error. First, expressions for the first-order evolution of the true background- and analysis-state errors will be derived. These expressions will then be related to the first-order evolution of background- and analysis-state perturbations in the ensemble system. The presentation is similar to that of Berre *et al.* (2006) but extended here to a nonlinear framework and tailored to account for particular features of our ensemble 3D-Var system.

B.1   First-order evolution of the true background- and analysis-state errors

As discussed in section 3 and illustrated in Fig. 1, the background state on a given 3D-Var cycle corresponds to the IAU-corrected state at the end of the previous cycle ($\mathbf{x}_c^b(t_0) = \mathbf{x}_{c-1}^a(t_N)$). For notational convenience, the index c will be ignored except when clarification is necessary.

The background state evolves from t_{i-1} and t_i according to (2) where $\mathbf{x}^b(t_0) = \mathbf{x}_c^b(t_0) = \mathbf{x}_{c-1}^a(t_N)$. Using the notation established in appendix A, the evolution of the true continuum state $\mathbf{x}_C^t(t_i)$ can be described by the equation

$$\mathbf{x}_C^t(t_i) \;=\; \mathscr{M}(t_i,t_{i-1})\big[\mathbf{x}_C^t(t_{i-1}),\mathbf{f}_{C,i}^t\big] \tag{34}$$

where $\mathscr{M}(t_i,t_{i-1})$ is the true continuum model operator from t_{i-1} to t_i, and $\mathbf{f}_{C,i}^t$ is the true continuum surface forcing vector acting from t_{i-1} to t_i. The evolution equation of the true resolved state $\mathbf{x}^t(t_i) \equiv \Pi_{(\mathbf{x})}\mathbf{x}_C^t(t_i)$ can be represented in terms of the discrete model operator $M(t_i,t_{i-1})$ and the true resolved forcing vector $\mathbf{f}_i^t \equiv \Pi_{(\mathbf{f})}\mathbf{f}_{C,i}^t$, where $\Pi_{(\mathbf{f})}$ is a projection operator from the atmospheric continuum onto the finite-dimensional subspace of the model forcing field, as

$$\mathbf{x}^t(t_i) \;=\; M(t_i,t_{i-1})\big[\mathbf{x}^t(t_{i-1}),\mathbf{f}_i^t\big] - \varepsilon_i^q \tag{35}$$

where ε_i^q is the model error. Following Cohn (1997) and Janjíc and Cohn (2006), ε_i^q can be neatly expressed as the sum $\varepsilon_i^q = \varepsilon_i^{qd} + \varepsilon_i^{qu}$ where

$$\varepsilon_i^{qd} \;=\; \big(M(t_i,t_{i-1})-\Pi_{(\mathbf{x})}\mathscr{M}(t_i,t_{i-1})\big)\big[\mathbf{x}^t(t_{i-1}),\mathbf{f}_i^t\big] \tag{36}$$

is the model error due to discretizaton, and

$$\varepsilon_i^{qu} \;=\; -\Pi_{(\mathbf{x})}\mathscr{M}(t_i,t_{i-1})\big[\mathbf{x}_C^t(t_{i-1})-\mathbf{x}^t(t_{i-1}),\mathbf{f}_{C,i}^t-\mathbf{f}_i^t\big] \tag{37}$$

is the model error due to the unresolved scales. Notice that our definition of model error through (36) and (37) does not include the contribution from the surface forcing field error

$$\varepsilon_i^f \;=\; \mathbf{f}_i-\mathbf{f}_i^t \tag{38}$$

which is treated separately in what follows. The forcing errors include errors inherent in the (re)analysis procedure used to produce the atmospheric fluxes as well as errors associated with the interpolation procedure used to map the fluxes onto the model grid and time step.

An equation for the time evolution of the background error,

$$\varepsilon^b(t_i) = \mathbf{x}^b(t_i) - \mathbf{x}^t(t_i) \tag{39}$$

can be derived by subtracting (35) from (2) to yield

$$\mathbf{x}^b(t_i) - \mathbf{x}^t(t_i) = M(t_i, t_{i-1})\Big[\mathbf{x}^b(t_{i-1}), \mathbf{f}_i\Big] - M(t_i, t_{i-1})\big[\mathbf{x}^t(t_{i-1}), \mathbf{f}_i^t\big] + \varepsilon_i^q. \tag{40}$$

Expanding the second term on the right-hand side of (40) about $\mathbf{x}^b(t_{i-1})$ and $\mathbf{f}_i$, and using (38) and (39), yields, to first order,

$$\varepsilon^b(t_i) \approx \mathbf{M}_{\mathbf{x}^b}(t_i, t_{i-1})\,\varepsilon^b(t_{i-1}) + \varepsilon_i^p$$

$$\approx \mathbf{M}_{\mathbf{x}^b}(t_i, t_0)\,\varepsilon^b(t_0) + \sum_{j=1}^{i} \mathbf{M}_{\mathbf{x}^b}(t_i, t_j)\,\varepsilon_j^p \tag{41}$$

where

$$\varepsilon_i^p = \mathbf{M}_{\mathbf{f}}(t_i, t_{i-1})\,\varepsilon_i^f + \varepsilon_i^q \tag{42}$$

is the total model error at time t_i. Here, $\mathbf{M}_{\mathbf{x}^b}(t_i, t_{i-1}) \equiv \partial M/\partial \mathbf{x}|_{\mathbf{x}=\mathbf{x}^b(t_{i-1})}$, $\mathbf{M}_{\mathbf{x}^b}(t_i, t_j) \equiv \mathbf{M}_{\mathbf{x}^b}(t_i, t_{i-1}) \cdots \mathbf{M}_{\mathbf{x}^b}(t_{j+1}, t_j)$, with $\mathbf{M}_{\mathbf{x}^b}(t_i, t_i) \equiv \mathbf{I}$, and $\mathbf{M}_{\mathbf{f}}(t_i, t_{i-1}) \equiv \partial M/\partial \mathbf{f}|_{\mathbf{f}=\mathbf{f}_i}$.

The assimilation method transforms the innovation vector, $\mathbf{d} = (..., \mathbf{d}_i^T, ...)^T$, into an analysis increment. By minimizing the 3D-Var FGAT cost function exactly, the analysis increment can be expressed as

$$\delta \mathbf{x}^a = \mathbf{K}\mathbf{d} \tag{43}$$

where

$$\mathbf{K} = \mathbf{B}\mathbf{H}^T\big(\mathbf{H}\mathbf{B}\mathbf{H}^T + \mathbf{R}\big)^{-1} \tag{44}$$

is the so-called Kalman gain matrix, $\mathbf{B}$ and $\mathbf{R}$ being the *prescribed* background and observation error covariance matrices detailed in section 3. The innovation vector can be expressed in terms of the background error (Eq. 39) and observation error (Eqs. (24) and (25)) by noting that

$$\mathbf{d}_i = \mathbf{y}_i^o - \mathbf{H}_i\mathbf{x}^b(t_i) = \mathbf{y}_i^o - \mathbf{H}_i\mathbf{x}^t(t_i) + \mathbf{H}_i\mathbf{x}^t(t_i) - \mathbf{H}_i\mathbf{x}^b(t_i) = \varepsilon_i^o - \mathbf{H}_i\varepsilon^b(t_i). \tag{45}$$

The analysis increment is applied to the model using IAU as described by (10). The first-order evolution of the analysis error,

$$\varepsilon^a(t_i) = \mathbf{x}^a(t_i) - \mathbf{x}^t(t_i), \tag{46}$$

is obtained by subtracting (35) from (10) to yield

$$\mathbf{x}^a(t_i) - \mathbf{x}^t(t_i) = M(t_i, t_{i-1})[\mathbf{x}^a(t_{i-1}), \mathbf{f}_i] + F_i\delta\mathbf{x}^a - M(t_i, t_{i-1})\big[\mathbf{x}^t(t_{i-1}), \mathbf{f}_i^t\big] + \varepsilon_i^q. \tag{47}$$

Expanding the third term on the right-hand side of (47) about $\mathbf{x}^a(t_{i-1})$ and $\mathbf{f}_i$ and using (42) gives, to first order,

$$\varepsilon^a(t_i) \approx \mathbf{M}_{\mathbf{x}^a}(t_i, t_{i-1})\,\varepsilon^a(t_{i-1}) + F_i\delta\mathbf{x}^a + \varepsilon_i^p$$

$$\approx \mathbf{M}_{\mathbf{x}^a}(t_i, t_0)\,\varepsilon^b(t_0) + \sum_{j=1}^{i} \mathbf{M}_{\mathbf{x}^a}(t_i, t_j)\left[F_j\delta\mathbf{x}^a + \varepsilon_j^p\right], \tag{48}$$

where $\varepsilon^b(t_0) = \varepsilon_c^b(t_0) = \varepsilon_{c-1}^a(t_N)$. Equation (48) is similar to (41) for the background error but employs a different linearization state ($\mathbf{x}^a(t_i)$ instead of $\mathbf{x}^b(t_i)$) and includes the analysis increment as an extra component in the model error term.

B.2 Ensemble representation of background- and analysis-state errors

Let the index l denote a particular ensemble member on a given cycle, and let $\tilde{\varepsilon}_l^b(t_0)$, $\tilde{\varepsilon}_{l,i}^f$, $\tilde{\varepsilon}_{l,i}^q$ and $\tilde{\varepsilon}_{l,i}^o$ define a set of perturbations to the system input parameters such that

$$
\begin{align}
\mathbf{x}_l^b(t_0) &= \mathbf{x}^b(t_0) + \tilde{\varepsilon}_l^b(t_0), & \tilde{\varepsilon}_l^b(t_0) &\sim N(0,\widetilde{\mathbf{P}}^b(t_0)), \tag{49}\\
\mathbf{f}_{l,i} &= \mathbf{f}_i + \tilde{\varepsilon}_{l,i}^f, & \tilde{\varepsilon}_{l,i}^f &\sim N(0,\widetilde{\mathbf{F}}_i), \tag{50}\\
\mathbf{q}_{l,i} &= \tilde{\varepsilon}_{l,i}^q, & \tilde{\varepsilon}_{l,i}^q &\sim N(0,\widetilde{\mathbf{Q}}_i), \tag{51}\\
\mathbf{y}_{l,i}^o &= \mathbf{y}_i^o + \tilde{\varepsilon}_{l,i}^o, & \tilde{\varepsilon}_{l,i}^o &\sim N(0,\widetilde{\mathbf{R}}_i), \tag{52}
\end{align}
$$

where $\tilde{\varepsilon} \sim N(0,\mathbf{A})$ means normally distributed with $E[\tilde{\varepsilon}] = 0$ and $E[\tilde{\varepsilon}\tilde{\varepsilon}^T] = \mathbf{A}$. From (2) and (10), the equations describing the time-evolution of the perturbed background state $\mathbf{x}_l^b(t_i)$ and perturbed analysis state $\mathbf{x}_l^a(t_i)$ can be written as

$$
\begin{align}
\mathbf{x}_l^b(t_i) &= M(t_i,t_{i-1})\left[\mathbf{x}_l^b(t_{i-1}),\mathbf{f}_{l,i}\right] + \mathbf{q}_{l,i}, \tag{53}\\
\mathbf{x}_l^a(t_i) &= M(t_i,t_{i-1})[\mathbf{x}_l^a(t_{i-1}),\mathbf{f}_{l,i}] + F_i\,\delta\mathbf{x}_l^a + \mathbf{q}_{l,i} \tag{54}
\end{align}
$$

where $\mathbf{x}_l^a(t_0) = \mathbf{x}_l^b(t_0)$, and $\delta\mathbf{x}_l^a = \mathbf{K}\,\mathbf{d}_l$, with $\mathbf{d}_l = (...,\mathbf{d}_{l,i}^T,...)^T$ and $\mathbf{d}_{l,i} = \mathbf{y}_{l,i}^o - \mathbf{H}\mathbf{x}_l^b(t_i)$, is the analysis increment produced using the perturbed observations and perturbed background trajectory of ensemble member l.

Subtracting (2) from (53) and (10) from (54), and linearizing terms, gives

$$
\tilde{\varepsilon}_l^b(t_i) \approx \mathbf{M}_{\mathbf{x}^b}(t_i,t_0)\,\tilde{\varepsilon}_l^b(t_0) + \sum_{j=1}^{i}\mathbf{M}_{\mathbf{x}^b}(t_i,t_j)\,\tilde{\varepsilon}_{l,j}^p, \tag{55}
$$

$$
\tilde{\varepsilon}_l^a(t_i) \approx \mathbf{M}_{\mathbf{x}^a}(t_i,t_0)\,\tilde{\varepsilon}_l^b(t_0) + \sum_{j=1}^{i}\mathbf{M}_{\mathbf{x}^a}(t_i,t_j)\left[F_j\,\delta\tilde{\mathbf{x}}_l^a + \tilde{\varepsilon}_{l,j}^p\right] \tag{56}
$$

where $\tilde{\varepsilon}_{l,i}^p = \mathbf{M}_{\mathbf{f}}(t_i,t_{i-1})\,\tilde{\varepsilon}_{l,i}^f + \tilde{\varepsilon}_{l,i}^q$, $\delta\tilde{\mathbf{x}}_l^a = \mathbf{K}\,\tilde{\mathbf{d}}_l$, $\tilde{\mathbf{d}}_l = (...,\tilde{\mathbf{d}}_{l,i}^T,...)^T$ and $\tilde{\mathbf{d}}_{l,i} = \tilde{\varepsilon}_{l,i}^o - \mathbf{H}\tilde{\varepsilon}_l^b(t_i)$. Comparing (55) and (56) with (41) and (48) shows that the ensemble perturbations, $\tilde{\varepsilon}_l^b(t_i)$ and $\tilde{\varepsilon}_l^a(t_i)$, and the true errors $\varepsilon^b(t_i)$ and $\varepsilon^a(t_i)$, obey identical first-order evolution equations. Furthermore, if the covariance matrices of the input perturbations in (49)–(52) are equal to the covariance matrices of the true errors, $\widehat{\mathbf{P}}^b(t_0) \equiv E[\varepsilon^b(t_0)(\varepsilon^b(t_0))^T]$, $\widehat{\mathbf{F}}_i \equiv E[\varepsilon_i^f(\varepsilon_i^f)^T]$, $\widehat{\mathbf{Q}}_i \equiv E[\varepsilon_i^q(\varepsilon_i^q)^T]$ and $\widehat{\mathbf{R}}_i \equiv E[\varepsilon_i^o(\varepsilon_i^o)^T]$, then it follows from (55) and (56) that the evolving covariance matrices $\widetilde{\mathbf{P}}^b(t_i) = E[\tilde{\varepsilon}_l^b(t_i)(\tilde{\varepsilon}_l^b(t_i))^T]$ and $\widetilde{\mathbf{P}}^a(t_i) = E[\tilde{\varepsilon}_l^a(t_i)(\tilde{\varepsilon}_l^a(t_i))^T]$ will be identical, to first order, to those of the true errors $\widehat{\mathbf{P}}^b(t_i) \equiv E[\varepsilon^b(t_i)(\varepsilon^b(t_i))^T]$ and $\widehat{\mathbf{P}}^a(t_i) \equiv E[\varepsilon^a(t_i)(\varepsilon^a(t_i))^T]$.

Of particular interest here is the covariance matrix $\widetilde{\mathbf{P}}^a(t_N) = E[\tilde{\varepsilon}_l^a(t_N)(\tilde{\varepsilon}_l^a(t_N))^T]$ of the analysis-state error $\tilde{\varepsilon}^a(t_N)$ at the end of the cycle since this matrix should be used to define the background-error covariance matrix for the next cycle (see Fig. 3): $\widetilde{\mathbf{P}}^a(t_N) = \widetilde{\mathbf{P}}_c^a(t_N) = \widetilde{\mathbf{P}}_{c+1}^b(t_0)$. This matrix can be estimated from a sample of L perturbed analysis states as

$$
\widetilde{\mathbf{P}}^a(t_N) \approx \frac{1}{L-1}\sum_{l=1}^{L}\left(\mathbf{x}_l^a(t_N) - \mathbf{x}^a(t_N)\right)\left(\mathbf{x}_l^a(t_N) - \mathbf{x}^a(t_N)\right)^T \tag{57}
$$

where each $\mathbf{x}_l^a(t_N)$ is generated by perturbing the system input parameters as in (49)–(52). Rather than using (57), Fisher (2003), Žagar *et al.* (2005) and Berre *et al.* (2006) suggest estimating $\widetilde{\mathbf{P}}^a(t_N)$ from differences between ensemble members. Assuming that the errors of the different members are mutually uncorrelated then

$$
\begin{align}
\widetilde{\mathbf{P}}^a(t_N) &= \frac{1}{2}E[(\tilde{\varepsilon}_l^a(t_N) - \tilde{\varepsilon}_{l+1}^a(t_N))(\tilde{\varepsilon}_l^a(t_N) - \tilde{\varepsilon}_{l+1}^a(t_N))^T]\\
&\approx \frac{1}{2(L-1)}\sum_{l=0}^{L}\left(\mathbf{x}_l^a(t_N) - \mathbf{x}_{l+1}^a(t_N)\right)\left(\mathbf{x}_l^a(t_N) - \mathbf{x}_{l+1}^a(t_N)\right)^T \tag{58}
\end{align}
$$

where $\mathbf{x}_{L+1}^a(t_N) = \mathbf{x}_0^a(t_N) = \mathbf{x}^a(t_N)$. The multiplicative factor $1/2$ arises since ensemble members are effectively used twice in (58). For historical reasons, (58) rather than (57) has been used in this study.

References

[1] E. Andersson, M. Fisher, R. Munro, and A. McNally. Diagnosis of background errors for radiances and other observable quantities in a variational data assimilation system, and the explanation of a case of poor convergence. *Quart. J. Roy. Meteor. Soc.*, 126:1455–1472, 2000.

[2] M. A. Balmaseda, D. Dee, A. Vidard, and D. L. T. Anderson. A multivariate treatment of bias for sequential data assimilation: Application to the tropical oceans. *Quart. J. Roy. Meteor. Soc.*, 133:167–179, 2007.

[3] M. A. Balmaseda, A. Vidard, and D. L. T. Anderson. The ECMWF ocean analysis system: ORA-S3. *Mon. Wea. Rev.*, In press, 2008.

[4] R. J. Barlow. *Statistics: A Guide to the Use of Statistical Methods in the Physical Sciences*. John Wiley, Chichester, UK, 1989.

[5] D. W. Behringer, M. Ji, and A. Leetmaa. An improved coupled model for ENSO prediction and implications for ocean initialization. Part I: The ocean data assimilation system. *Mon. Wea. Rev.*, 126:1013–1021, 1998.

[6] M. Belo Pereira and L. Berre. The use of an ensemble approach to study the background error covariances in a global NWP model. *Mon. Wea. Rev.*, 134:2466–2489, 2006.

[7] L. Berre, S. E. Ştefănescu, and M. Belo Pereira. The representation of the analysis effect in three error simulation techniques. *Tellus*, 58A:196–209, 2006.

[8] L. Berre, O. Pannekoucke, G. Desroziers, S. E. Ştefănescu, B. Chapnik, and L. Raynaud. A variational assimilation ensemble and the spatial filtering of its error covariances: increase of sample size by local spatial averaging. In *Proceedings of the ECMWF Workshop on Flow Dependent Aspects of Data Assimilation*, pages 151–168. ECMWF, 11-13 June 2007.

[9] S. C. Bloom, L. L. Takacs, A. M. da Silva, and D. Ledvina. Data assimilation using incremental analysis updates. *Mon. Wea. Rev.*, 124:1256–1271, 1996.

[10] M. Buehner. Ensemble-derived stationary and flow-dependent background-error covariances: Evaluation in a quasi-operational NWP setting. *Quart. J. Roy. Meteor. Soc.*, 131:1013–1044, 2005.

[11] M. Buehner and M. Charron. Spectral and spatial localization of background-error correlations for data assimilation. *Quart. J. Roy. Meteor. Soc.*, 133:615–630, 2007.

[12] J. A. Carton and A. Santorelli. Global decadal upper ocean heat content as viewed in nine analyses. *Submitted to J. of Climate*, 2008.

[13] S. E. Cohn. An introduction to estimation theory. *J. Met. Soc. Japan*, 75:257–288, 1997.

[14] M. E. Conkright, J. I. Antonov, O. Baranova, T. P. Boyer, H. E. Garcia, R. Gelfeld, D. Johnson, R. A. Locarnini, P. P. Murphy, T. D. O'Brien, I. Smolyar, and C. Stephens. *World Ocean Database 2001 Volume 1: Introduction*, volume NOAA Atlas NESDIS 29. U.S. Gov. Printing Office, Wash., D.C., 2002.

[15] P. Courtier, J.-N. Thépaut, and A. Hollingsworth. A strategy for operational implementation of 4D-Var, using an incremental approach. *Quart. J. Roy. Meteor. Soc.*, 120:1367–1387, 1994.

[16] M. Davey, M. Huddleston, B. Ingleby, K. Haines, P. Y. Le Traon, A. T. Weaver, J. Vialard, D. Anderson, A. Troccoli, A. Vidard, G. Burgers, O. Leeuwenburgh, A. Bellucci, S. Masina, L. Bertino, and P. Korn. Multi-model multi-method multi-decadal ocean analyses from the ENACT project. *CLIVAR Exchanges 38*, 11:22–25, 2006.

[17] D. P. Dee and R. Todling. Data assimilation in the presence of forecast bias: The GEOS moisture analysis. *Mon. Wea. Rev.*, 128:3268–3282, 2000.

[18] J. C. Derber and F. Bouttier. A reformulation of the background error covariance in the ECMWF global data assimilation system. *Tellus*, 51A:195–221, 1999.

[19] G. Desroziers, L. Berre, B. Chapnik, and P. Poli. Diagnosis of observation, background and analysis-error statistics in observation space. *Quart. J. Roy. Meteor. Soc.*, 131:3385–3396, 2005.

[20] G. Evensen. *Data Assimilation: The Ensemble Kalman Filter*. Springer, 2007.

[21] M. Fisher. Minimization algorithms for variational data assimilation. In *Seminar on Recent Developments in Numerical Methods for Atmospheric Modelling*, pages 364–385. ECMWF, 7-11 September 1998.

[22] M. Fisher. Background error covariance modelling. In *Proceedings of the ECMWF Seminar on Recent Developments in Data Assimilation for Atmosphere and Ocean*, pages 45–63. ECMWF, 8-12 September 2003.

[23] L. L. Fu, I. Fukumori, and R. N. Miller. Fitting dynamic models to the Geosat sea level observations in the tropical Pacific Ocean. Part II: A linear, wind-driven model. *J. Phys. Oceanogr.*, 23:2162–2181, 1993.

[24] I. Fukumori. Data assimilation by models. In L. L. Fu and A. Cazenave, editors, *Satellite Altimetry and Earth Sciences: A Handbook of Techniques and Applications*, pages 237–265. Academic Press, 2000. ISBN-10 0122695453.

[25] P. R. Gent and J. C. McWilliams. Isopycnal mixing in ocean circulation models. *J. Phys. Oceanogr.*, 20:150–155, 1990.

[26] T. M. Hamill and C. Snyder. A hybrid ensemble kalman fitler-3D variational analysis scheme. *Mon. Wea. Rev.*, 128:2905–2919, 2000.

[27] T. M. Hamill and J. S. Whitaker. Accouting for the error due to unresolved scales in ensemble data assimilation: A comparison of different approaches. *Mon. Wea. Rev.*, 133:3132–3147, 2005.

[28] P. L. Houtekamer and H. L. Mitchell. A sequential ensemble Kalman filter for atmospheric data assimilation. *Mon. Wea. Rev.*, 129:123–137, 2001.

[29] P. L. Houtekamer and H. L. Mitchell. Ensemble Kalman filtering. *Quart. J. Roy. Meteor. Soc.*, 131:3269–3289, 2005.

[30] B. Ingleby and M. Huddleston. Quality control of ocean temperature and salinity profiles - historical and real-time data. *J. Mar. Sys.*, 65:158–175, 2007.

[31] T. Janjíc and S. E. Cohn. Treatment of observation error due to unresolved scales in atmospheric data assimilation. *Mon. Wea. Rev.*, 134:2900–2915, 2006.

[32] G. C. Johnson, B. M. Sloyan, W. S. Kessler, and K. E. McTaggart. Direct measurements of upper ocean currents and water properties across the tropical Pacific during the 1990's. *Prog. Oceanogr.*, 52:31–36, 2002.

[33] P. W. Jones. A user's guide for SCRIP: A spherical coordinate remapping and interpolation package. Technical report, Los Alamos National Laboratory, 1998.

[34] C. L. Keppenne and M. M. Rienecker. Initial testing of a massively parallel Ensemble Kalman Filter with the Poseidon isopycnal ocean general circulation model. *Mon. Wea. Rev.*, 130:2951–2965, 2002.

[35] G. S. E. Lagerloef, G. T. Mitchum, R. B. Lukas, and P. P. Niiler. Tropical Pacific near-surface currents estimated from altimeter, wind, and drifter data. *J. Geophys. Res.*, 104:23313–23326, 1999.

[36] O. Leeuwenburgh. Validation of an EnKF system for OGCM initialization assimilating temperature, salinity, and surface height measurements. *Mon. Wea. Rev.*, 135:125–139, 2007.

[37] A. C. Lorenc. Modelling of error covariances by 4D-Var data assimilation. *Quart. J. Roy. Meteor. Soc.*, 129:3167–3182, 2003.

[38] A. C. Lorenc. The potential of the Ensemble Kalman Filter for NWP – a comparison with 4D-Var. *Quart. J. Roy. Meteor. Soc.*, 129:3183–3203, 2003.

[39] G. Madec, P. Delecluse, M. Imbard, and C. Levy. OPA 8.1 Ocean General Circulation Model reference manual. Notes du pôle de modélisation, Institut Pierre Simon Laplace (IPSL), France, 1998.

[40] D. Menemenlis and M. Chechelnitsky. Error estimates for an ocean general circulation model from altimeter and acoustic tomography data. *Mon. Wea. Rev.*, 128:763–785, 2000.

[41] P. R. Oke, P. Sakov, and S. P. Corney. Impacts of localisation in the EnKF and EnOI: experiments with a small model. *Ocean Dynamics*, 57:32–45, 2007.

[42] E. Ott, B. R. Hunt, I. Szunyogh, A. V. Zimin, E. J. Kostelich, M. Corazza, E. Kalnay, D. J. Patil, and J. A. Yorke. A local ensemble Kalman filter for atmospheric data assimilation. *Tellus*, 56A:415–428, 2004.

[43] O. Pannekoucke, L. Berre, and G. Desroziers. Background error correlation length-scale estimates and their sampling statistics. *Quart. J. Roy. Meteor. Soc.*, 134:497–508, 2008.

[44] O. Pannekoucke and S. Massart. Estimation of the local diffusion tensor and normalization for heterogeneous correlation modeling using a diffusion equation. *Submitted to Quart. J. Roy. Meteor. Soc.*, 2008.

[45] R. J. Purser, W.-S. Wu, D. F. Parrish, and N. M. Roberts. Numerical aspect of the application of recursive filters to variational statistical analysis. Part I: Spatially homogeneous and isotropic Gaussian covariances. *Mon. Wea. Rev.*, 131:1524–1535, 2003.

[46] R. Reynolds, N. Rayner, T. Smith, D. Stokes, and W. Wang. An improve in situ and satellite SST analysis for climate. *J. Clim.*, 15:1609–1625, 2002.

[47] S. Ricci, A. T. Weaver, J. Vialard, and P. Rogel. Incorporating state-dependent temperature-salinity constraints in the background-error covariance of variational ocean data assimilation. *Mon. Wea. Rev.*, 133:317–338, 2005.

[48] G. Roullet and G. Madec. Salt conservation, free surface and varying volume: a new formulation for Ocean GCMs. *J. Geophys. Res.*, 105:23927–23942, 2000.

[49] O. Talagrand. *A posteriori* verification of analysis and assimilation algorithms. In *Proceedings of the ECMWF Workshop on Diagnosis of Data Assimilation System*, pages 17–28, Reading, U-K, 2-4 November 1999. ECMWF.

[50] A. Troccoli and P. Kållberg. Precipitation correction in the ERA-40 reanalysis. ERA-40 Project Report Series 13, ECMWF, 2004.

[51] J. Tshimanga, S. Gratton, A. T. Weaver, and A. Sartenaer. Limited-memory preconditioners, with application to incremental four-dimensional variational data assimilation. *Quart. J. Roy. Meteor. Soc.*, 134:753–771, 2008.

[52] S. M. Uppala, P. W. Kållberg, A. J. Simmons, U. da Costa Bechtold, M. Fiorino, J. K. Gibson, J. Haseler, A. Hernandez, G. A. Kelly, X. Li, K. Onogi, S. Saarinen, N. Sokka, R. P. Allan, E. Andersson, K. Arpe, M. A. Balmaseda, A. C. M. Beljaars, L. van de Berg, J. Bidlot, N. Bormann, S. Caires, F. Chevallier, A. Dethof, M. Dragosavac, M. Fisher, M. Fuentes, S. Hagemann, E. Hólm, B. J. Hoskins, L. Isaksen, P. A. E. M. Janssen, R. Jenne, A. P. McNally, J.-F. Mahfouf, J.-J. Morcrette, N. A. Rayner, R. W. Saunders, P. Simon, A. Sterl, K. E. Trenberth, A. Untch, D. Vasiljevic, P. Viterbo, and J. Woollen. The ERA-40 reanalysis. *Quart. J. Roy. Meteor. Soc.*, 131:2961–3012, 2005.

[53] J. Vialard, A. T. Weaver, D. L. T. Anderson, and P. Delecluse. Three- and four-dimensional variational assimilation with a general circulation model of the tropical Pacific Ocean. Part II: Physical validation. *Mon. Wea. Rev.*, 131:1379–1395, 2003.

[54] A. T. Weaver and P. Courtier. Correlation modelling on the sphere using a generalized diffusion equation. *Quart. J. Roy. Meteor. Soc.*, 127:1815–1846, 2001.

[55] A. T. Weaver, C. Deltel, E. Machu, S. Ricci, and N. Daget. A multivariate balance operator for variational ocean data assimilation. *Quart. J. Roy. Meteor. Soc.*, 131:3605–3625, 2005.

[56] A. T. Weaver, J. Vialard, and D. L. T. Anderson. Three- and four-dimensional variational assimilation with a general circulation model of the tropical Pacific Ocean. Part I: Formulation, internal diagnostics and consistency checks. *Mon. Wea. Rev.*, 131:1360–1378, 2003.

[57] A. Weisheimer, F. Doblas-Reyes, P. Rogel, E. Da Costa, N. Keenlyside, M. Balmaseda, J. Murphy, D. Smith, M. Collins, B. Bhaskaran, and T. Palmer. Initialisation strategies for decadal hindcasts for the 1960-2005 period within the ENSEMBLES project. Tech. Memo 521, ECMWF, 2006.

[58] N. Žagar, E. Andersson, and M. Fisher. Balanced tropical data assimilation based on a study of equatorial waves in ECMWF short-range forecast errors. *Quart. J. Roy. Meteor. Soc.*, 131:987–1011, 2005.